Chemical Geology 432 (2016) 1–15

Contents lists available at ScienceDirect

Chemical Geology

journal homepage: www.elsevier.com/locate/chemgeo

Rapid lithospheric thinning of the North China Craton: New evidence from cretaceous mafic dikes in the Jiaodong Peninsula

Liang Ma [a], Shao-Yong Jiang [b,c,*], Albrecht W. Hofmann [d,e], Yi-Gang Xu [a], Bao-Zhang Dai [c], Ming-Lan Hou [f]

[a] State Key Laboratory of Isotope Geochemistry, Guangzhou Institute of Geochemistry, Chinese Academy of Sciences, Guangzhou 510640, China
[b] State Key Laboratory of Geological Processes and Mineral Resources, Collaborative Innovation Center for Exploration of Strategic Mineral Resources, Faculty of Earth Resource, China University of Geosciences, Wuhan 430074, China
[c] State Key Laboratory for Mineral Deposits Research, School of Earth Sciences and Engineering, Nanjing University, Nanjing 210093, China
[d] Max-Planck-Institut für Chemie, Postfach 3060, D-55020 Mainz, Germany
[e] Lamont-Doherty Earth Observatory of Columbia University, P.O. Box 1000, Palisades, NY 10964, USA
[f] Shandong Bureau of China Metallurgical Geology Bureau, Jinan 250014, China

ARTICLE INFO

Article history:
Received 17 October 2015
Received in revised form 22 March 2016
Accepted 29 March 2016
Available online 6 April 2016

Keywords:
Asthenospheric mantle
Mafic dikes
Mechanism of lithospheric thinning
North China Craton

ABSTRACT

The North China Craton is a classic case for the destruction of an ancient craton, in that it records the loss of more than 100 km of ancient refractory lithospheric mantle during the late Mesozoic and early Cenozoic. However, the mechanisms for this lithospheric thinning remain controversial in large part due to the lack of any systematic investigations of the Mesozoic asthenospheric mantle via its derived mafic rocks, which are key to understand the thinning processes. In this paper, we present detailed zircon U–Pb geochronology, elemental geochemistry, and Sr–Nd–Hf isotopic data for lamprophyres and diabase-porphyries of the Jiaodong Peninsula, in the eastern North China Craton in order to place constraints on models for lithospheric thinning. Our results show that the lamprophyres and diabase-porphyries are derived from the convective asthenospheric mantle via different degrees of partial melting, and that this mantle source was previously modified by carbonatitic liquids. Zircon LA-ICP-MS U–Pb dating suggests an emplacement age for these rocks of 123–121 Ma, the earliest evidence for asthenospherically-derived melts in the Jiaodong Peninsula so far. This emplacement age indicates that the thickness of the lithosphere in the Jiaodong Peninsula was relatively thin at that time. Co-occurrence of the asthenospheric and lithospheric mantle-derived mafic rocks as well as high-Mg adakites record a rapid transition from lithospheric to asthenospheric mantle sources, indicating that the lithosphere beneath the Jiaodong Peninsula was rapidly detached just prior to ca. 120 Ma. Lithospheric thinning of the North China Craton may have been initiated from the Jiaodong Peninsula and Bohai Sea and then propagated towards the interior of the craton.
© 2016 Elsevier B.V. All rights reserved.

1. Introduction

The North China Craton (NCC), one of the world's oldest cratons with an Archean nucleus of 2.5–3.8 Ga (Liu et al., 1992; Zhai and Santosh, 2011), underwent a dramatic lithospheric thinning during late Mesozoic and early Cenozoic times (Menzies et al., 1993; Menzies and Xu, 1998; Griffin et al., 1998; Fan et al., 2000; Xu, 2001; Xu et al., 2004a; Gao et al., 2002, 2004; Zheng et al., 2006; Yang and Li, 2008; Zhang et al., 2008a). This fundamental change in lithospheric architecture has attracted considerable attention over the last three decades, but the specific deep-level processes associated with the thinning of the lithosphere are still being actively debated. Thermo-mechanical–chemical erosion (e.g., Menzies et al., 1993; Griffin et al., 1998; Menzies and Xu, 1998; Xu, 2001; Xu et al., 2004a; Zheng et al., 2006, 2007) and rapid lithospheric delamination (e.g., Wu et al., 2003, 2005a; Yang et al., 2003; Gao et al., 2004; Jiang et al., 2010; Ma et al., 2014a) are two major hypotheses that have been suggested for the mode of lithospheric thinning. The former represents a slow thinning process lasting at least 100 Ma, whereas the latter marks a short event lasting about 10 Ma (Menzies et al., 2007; Ma et al., 2014a).

The asthenospheric mantle-derived mafic rocks are important indicators related to cratonic destruction, and study on these rocks can help us to resolve the above questions of timing and mechanism of lithospheric thinning. The thinning process is generally accompanied by upwelling of the convective asthenosphere and modification of the thermal structure of the lithosphere (Xu, 2006; Xu et al., 2009). During lithospheric extension, the source of magmas can shift from the lithosphere (i.e., enriched mantle) to the asthenosphere (Wu et al., 2008; Yang and Wu, 2009; Xu et al., 2009). Normally, the asthenosphere beneath an old craton cannot melt until the thickness of the lithosphere

* Corresponding author at: State Key Laboratory of Geological Processes and Mineral Resources, Collaborative Innovation Center for Exploration of Strategic Mineral Resources, Faculty of Earth Resource, China University of Geosciences, Wuhan 430074, China.
E-mail address: shyjiang@cug.edu.cn (S.-Y. Jiang).

http://dx.doi.org/10.1016/j.chemgeo.2016.03.027
0009-2541/© 2016 Elsevier B.V. All rights reserved.

is markedly thinned (e.g., Mckenzie and Bickle, 1988). Two key questions in constraining the mechanism of lithospheric thinning beneath the NCC are: (1) When did the magma source shift from lithospheric to asthenospheric mantle? (2) Was this transition a relatively "slow", or a "rapid" process?

In this study, we combined detailed zircon U–Pb geochronology with major and trace element geochemical and Sr–Nd–Hf isotopic studies on diabase-porphyry and lamprophyre dikes emplaced in the Jiaodong Peninsula. These results extend and complement our previous work on lamprophyre dikes from this region (Ma et al., 2014a). Whereas our previous work discussed the significance of essentially simultaneously emplaced lithosphere and asthenosphere-derived lamprophyres, we now focus on additional evidence from diabase porphyry dikes and their asthenospheric sources, and their relationship to asthenospherically-derived lamprophyres. Thus the chief aims of this study are: (1) to obtain the ages of these mafic rocks; (2) to interpret the nature of mantle sources; (3) and to obtain additional information on manner of lithospheric thinning beneath the NCC.

2. Geological setting and samples

The NCC is made up mainly of Neoarchean to Paleoproterozoic basement rocks overlain by Mesoproterozoic to Cenozoic unmetamorphosed cover (Zhai and Santosh, 2011; Jiang et al., 2013). The tectonic architecture of the NCC is defined by the Eastern Block, the Western Block and the intervening Trans-North China Orogen (Fig. 1a), on the base of age, lithological assemblage, tectonic evolution and metamorphic P-T-t paths (e.g., Zhao et al., 2001). It is bounded to the north by the southern margin of the late Paleozoic Central Asian Orogenic Belt and to the south by the Triassic Qingling–Dabie–Sulu UHP Orogenic Belt. To the east, the Paleo-Pacific plate started to subduct beneath Eurasian continent before Jurassic (Maruyama et al., 1997; Zhou and Li, 2000; Li and Li, 2007), and this subduction controlled the major tectonic and magmatic activities in eastern China during the Cretaceous (e.g., Sun et al., 2007). The present research focuses on the Jiaodong Peninsula (Fig. 1b), which located on the southeastern margin of the NCC and comprises two different terrains, the southeastern Sulu orogenic belt and the northwestern Jiaobei terrain, bounded by the Wulian–Mishan fault (Zhao et al., 2001). The Sulu orogenic belt was formed by the Triassic subduction of the Yangtze Block beneath the North China Block, and it contains the largest outcrop of UHP metamorphic rocks on Earth (e.g., Li et al., 1993; Jahn et al., 1996; Zheng et al., 2003). The Precambrian basement in the Jiaobei terrane is mainly composed of the Neoarchaean Jiaodong Group, the Paleoproterozoic Fenzishan and Jingshan groups, and the Neoproterozoic Penglai Group (e.g., Zhang et al., 2003a; Tang et al., 2007; Jahn et al., 2008). The Yanshanian granitoids intruded the Precambrian basement and have been grouped into two main suites: the Linglong granites (~160 Ma) and the Guojialing granodiorites (~130 Ma) (e.g., Wang et al., 1998; Qiu et al., 2002; Zhang et al., 2003a, 2010; Ma et al., 2013). Mafic to intermediate dikes, such as lamprophyre, diabase and diorite, intruded the Yanshanian granitoids and basement rocks. Available K–Ar, Ar–Ar and U–Pb ages for these dikes range from 132 to 113 Ma, with an age peak at ~120 Ma (Yang et al., 2004; Guo et al., 2004, 2005; Hu et al., 2007; Tan et al., 2008; Liu et al., 2008, 2009; Li et al., 2010; Ma et al., 2014a).

The diabase-porphyry and lamprophyre dikes in this study were collected from drill cores and underground shafts of the Jiaojia, Sizhuang, and Wangershan gold deposits, which are located in the NNE- to NE-trending Jiaojia-Xincheng fault zone in the northwestern part of the Jiaobei terrain. The diabase-porphyry rocks are melanocratic with typical ophitic texture and massive structure. The phenocrysts of the

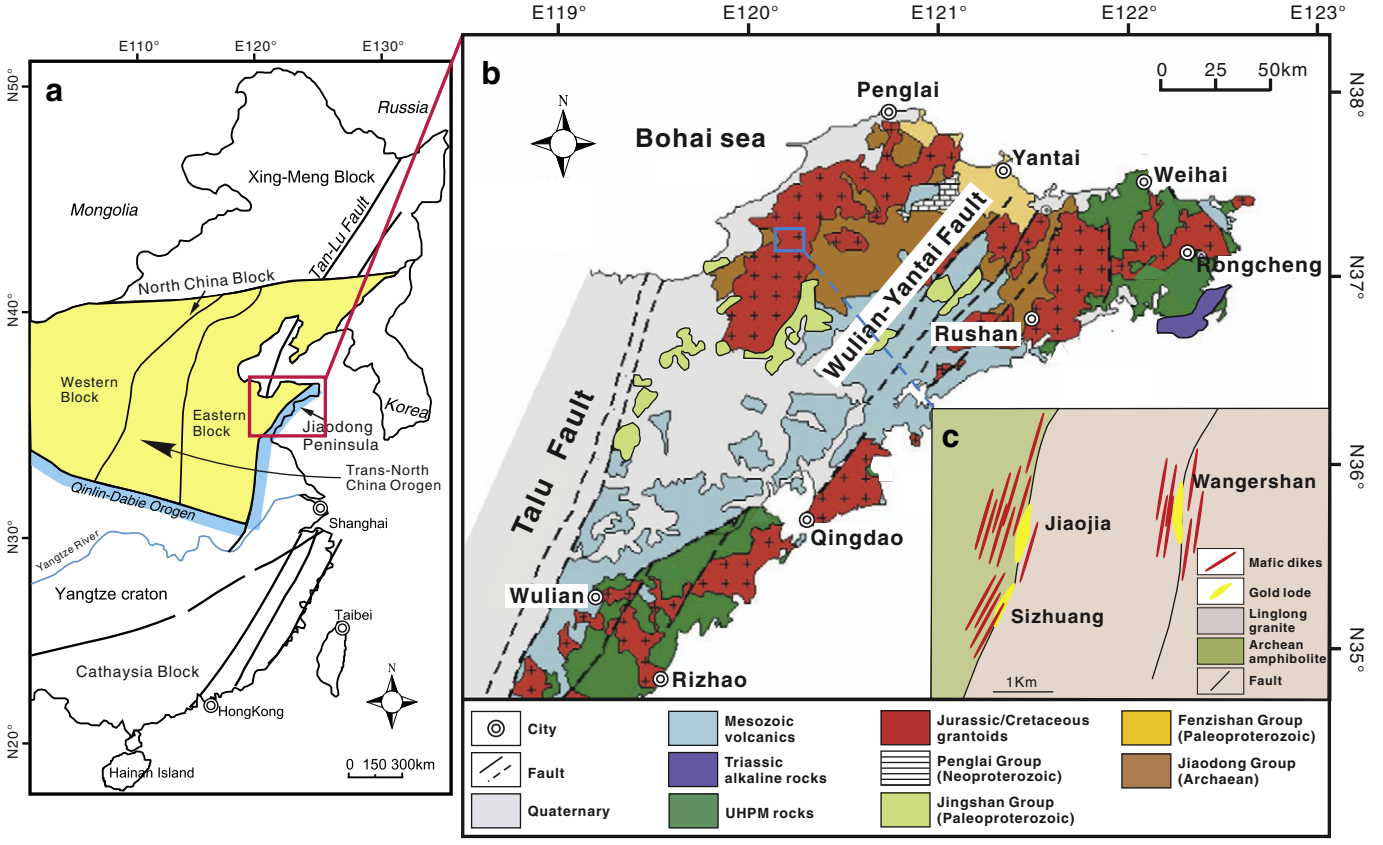

Fig. 1. (a) Simplified geological map showing eastern China and major tectonic units of the North China Craton (modified after Zhao et al., 2001 and Zeng et al., 2011). (b) Sketch map of the geology of the Jiaodong Peninsula (modified after Tang et al., 2006). (c) Geological map of the Jiaojia-Xincheng gold camp, with location of mafic dikes from the Jiaojia, Sizhuang, and Wangershan gold deposits.

diabase-porphyry consist dominantly of coarse, euhedral to subhedral clinopyroxene (~15%; by volume) and euhedral plagioclase (~10%). Rare olivine phenocrysts (~5%) are present in some samples, which are generally altered to serpentine and talc. Their groundmass consists of plagioclase (~35%), clinopyroxene (~25%), amphibole (~5%) and biotite (~5%) (Fig. 2a). Accessory minerals in the groundmass of the diabase-porphyry include apatite, zircon and magnetite. The lamprophyres are holocrystalline rocks with porphyritic texture, classified as spessartite according to the classification scheme of Woolley et al. (1996). The phenocrysts of lamprophyre contain mainly euhedral to subhedral clinopyroxene (~15%), olivine (~5%) and orthopyroxene (~5%), which are generally fresh, and the groundmass consists of amphibole (~35%), plagioclase (~30%), carbonate (~5%) and quartz (0–5%) (Fig. 2b). Accessory minerals in the groundmass of lamprophyre are magnetite, ilmenite, zircon and apatite. After petrographic examination, fifteen freshest samples (ten diabase-porphyries and five lamprophyres) were selected for elemental and Sr–Nd isotopic analyses. On two of the diabase-porphyry samples we conducted zircon U–Pb dating and in-situ Lu–Hf isotopic analyses.

3. Analytical methods

Measurements of whole-rock major and trace element abundances were conducted at the State Key Laboratory for Mineral Deposits Research, Nanjing University. Major elements were analyzed using a Jobin Yvon 38S ICP–AES, with analytical uncertainties better than 0.5%. For trace element analyses, about 50 mg of powdered sample was dissolved in high-pressure Teflon bombs using a HF + HNO_3 mixture. Rh was used as an internal standard to monitor signal drift during ICP-MS measurement. The trace elements were analyzed on a Finnigan Element II high-resolution inductively coupled plasma mass spectrometer (HR-ICP–MS), at an analytical precision of better than 10%. The USGS rock standards (GSP-1 and AGV-2) were used as calibration standards during the measurements. Our detailed analytical procedures for trace elements followed those of Gao et al. (2003). Sr and Nd isotopic analyses were performed using a Finnigan Triton TI thermal ionization mass spectrometer (TIMS) at the State Key Laboratory for Mineral Deposits Research, Nanjing University, following the procedures of Pu et al. (2004, 2005). About 100 mg powder of each sample was dissolved in Teflon beakers with HF + HNO_3 mixture acid. Complete separation of Sr was achieved by a combination of cation-exchange chromatography in H^+ form and pyridinium form with the DCTA complex. Nd was then separated from the REE fractions by cation-exchange resin using HIBA as eluent. The separated Sr sample was dissolved in 1 μl of 1 M HCl and then loaded with a TaF_5 solution onto W filament. The separated Nd sample was dissolved in 1 μl of 1 M HCl and then loaded with H_3PO_4 solution onto a Re double filament assembly. Sr–Nd isotopic compositions were normalized to $^{86}Sr/^{88}Sr = 0.1194$ and $^{146}Nd/^{144}Nd = 0.7219$, respectively. Measurements of NBS987 Sr standard yielded $^{87}Sr/^{86}Sr = 0.710255 \pm 0.000011$ (2σ), and JNdi-1 Nd standard yielded $^{143}Nd/^{144}Nd = 0.512122 \pm 0.000009$ (2σ).

Zircon LA-ICP-MS U–Pb analyses were carried out using an Agilent 7500 ICP-MS equipped with a New Wave Research 213 nm laser ablation system at State Key Laboratory for Mineral Deposits Research, Nanjing University. Helium was used as carrier gas to transport the ablated sample to the ICP-MS. During the analyses, a beam spot size of 30 μm, a laser frequency of 5 Hz and an energy of 10 to 20 J/cm^2 were used. Each run comprised of 10 unknown sample spot analyses, bracketed by four GJ-1 and two Mud Tank zircon standards. Detailed analytical procedures are similar to those summarized by Jackson et al. (2004). The raw ICP-MS data were exported in ASCII format and processed using GLITTER. Common Pb contents were evaluated using the method described by Andersen (2002). The age calculations and plotting of Concordia diagrams were made using Isoplot v. 3.23 (Ludwig, 2003). In-situ zircon Hf isotope analysis was carried out using a New Wave UP213 laser-ablation system, attached to a Neptune multi-collector ICP-MS at Institute of Mineral Resources, Chinese Academy of Geological Sciences, Beijing. Instrumental conditions and data acquisition were comprehensively described by Hou et al. (2007a). A stationary spot was used for the present analyses, with a beam diameter of 55 μm. Helium was used as carrier gas to transport the ablated sample from the laser-ablation cell into the ICP-MS torch via a mixing chamber where it was mixed with Argon. In order to correct the isobaric interferences of ^{176}Lu and ^{176}Yb on ^{176}Hf, $^{176}Lu/^{175}Lu = 0.02658$ and $^{176}Yb/^{173}Yb = 0.796218$ ratios were determined, after Chu et al. (2002). For instrumental mass bias correction Yb isotope ratios were normalized to $^{172}Yb/^{173}Yb = 1.35274$ (Chu et al., 2002) and Hf isotope ratios to $^{179}Hf/^{177}Hf = 0.7325$ using an exponential law. The mass bias behavior of Lu was assumed to follow that of Yb, mass bias correction protocols details were described by Hou et al. (2007a). Zircon GJ1 was used as the reference standard, with a weighted mean $^{176}Hf/^{177}Hf$ ratio of 0.282009 ± 0.000011 (2σ, n = 10) during the period of sample analyses. It is not distinguishable from a weighted mean $^{176}Hf/^{177}Hf$ ratio of 0.282013 ± 0.000019 (2σ) from in-situ analysis by Elhlou et al. (2006).

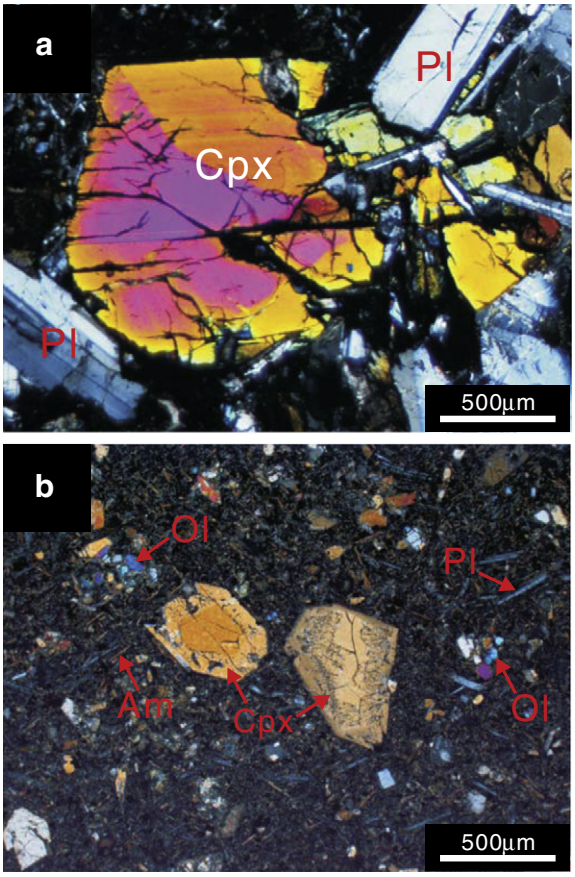

Fig. 2. Petrographic characteristics of the mafic dikes: (a) diabase-porphyries, mainly composed of plagioclase, clinopyroxene, orthopyroxene, olivine and amphibole; (b) lamprophyres, mainly composed of olivine, clinopyroxene, plagioclase and amphibole. Ol–olivine; Cpx–clinopyroxenes; Pl–plagioclase; Am–amphibole.

4. Results

4.1. Whole-rock geochemistry

The results of whole-rock major and trace element concentrations as well as Sr–Nd isotope analyses for the lamprophyres and diabase-porphyries are listed in Table 1. Data for lamprophyre samples JJHT-1 to JJHT-10 were previously published by Ma et al. (2014a) but are also included here for the readers' convenience and completeness. Major

Table 1
Whole-rock geochemistry of the diabase-porphyry and lamprophyre in the Jiaodong Peninsula.

Sample	Diabase-porphyrite									
	DP-1	DP-2	DP-3	DP-4	DP-5	DP-6	DP-7	DP-8	DP-9	DP-10
Location	37°24′28.8″ 120°8′39.5″	37°23′52.8″ 120°8′1.8″	37°23′53.1″ 120°8′1.9″	37°24′27.5″ 120°8′39.3″	37°24′1.2″ 120°8′8.6″	37°24′28.8″ 120°8′39.5″	37°24′28.8″ 120°8′39.5″	37°24′28.8″ 120°8′39.5″	37°23′52.8″ 120°8′1.8″	37°23′52.8″ 120°8′1.8″
Depth	345 m	131 m	59 m	360 m	264 m	317 m	187 m	147 m	195 m	258 m
SiO_2	48.50	47.47	49.21	48.27	46.91	47.74	48.23	48.47	47.34	47.84
TiO_2	2.21	2.20	2.19	2.73	2.11	2.49	2.51	2.61	2.36	2.34
Al_2O_3	14.87	15.36	14.45	16.92	14.28	16.03	16.14	15.98	15.77	16.52
TFe_2O_3	11.78	13.27	11.69	12.99	12.74	12.22	12.23	12.19	11.90	11.58
FeO	6.88	6.22	5.51	7.84	7.81	6.42	6.59	5.57	7.11	7.13
Fe_2O_3	4.13	6.36	5.57	4.28	4.06	5.09	4.90	6.01	3.99	3.65
MnO	0.21	0.18	0.18	0.18	0.22	0.17	0.20	0.22	0.19	0.17
MgO	6.81	5.97	7.37	3.92	8.26	5.18	3.86	4.38	4.86	4.68
CaO	9.09	8.71	7.85	7.64	9.54	8.06	9.18	8.82	8.43	8.48
Na_2O	3.25	3.21	3.06	4.07	3.14	3.69	3.12	3.62	3.75	3.16
K_2O	1.10	1.01	1.10	1.91	1.00	1.60	1.60	1.69	1.32	1.43
P_2O_5	0.54	0.45	0.52	0.64	0.43	0.51	0.52	0.67	0.44	0.51
LOI	2.28	2.78	3.06	1.82	2.12	2.94	3.25	2.16	4.28	3.82
Total	99.9	99.9	100.1	100.2	99.9	99.9	100.1	100.2	99.9	99.7
Mg#	54	47	56	38	56	46	39	42	45	45
La	29.1	27.6	32.2	31.6	31.9	36.7	36.6	38.4	33.6	33.4
Ce	75.7	74.7	70.8	87.5	63.3	76.6	80.8	82.5	74.1	67.7
Pr	6.87	6.95	8.70	8.10	8.39	9.23	9.50	9.37	8.91	8.23
Nd	29.60	29.31	34.93	33.91	35.46	38.81	39.36	38.13	38.79	30.81
Sm	6.18	5.78	7.56	6.59	7.07	7.68	7.64	8.15	7.66	6.95
Eu	2.10	2.10	2.41	2.23	2.23	2.41	2.38	2.39	2.48	2.06
Gd	5.28	5.82	7.04	6.44	6.55	7.12	6.99	6.97	7.34	6.41
Tb	0.84	0.88	0.91	0.94	0.83	0.94	0.94	0.94	0.95	0.85
Dy	5.36	5.35	5.35	5.66	5.14	5.63	5.50	5.67	5.89	4.46
Ho	0.91	0.90	1.06	0.94	0.96	1.06	1.02	1.13	1.07	0.86
Er	2.56	2.42	2.55	2.49	2.50	2.57	2.53	2.72	2.62	2.24
Tm	0.37	0.34	0.34	0.39	0.31	0.34	0.34	0.34	0.35	0.31
Yb	1.81	1.81	2.04	2.01	1.93	2.08	2.10	2.14	2.10	1.97
Lu	0.29	0.28	0.30	0.31	0.28	0.31	0.30	0.31	0.30	0.23
Rb	20.91	15.37	20.43	31.17	15.17	30.88	27.87	29.93	22.24	31.14
Ba	465	381	484	597	320	478	455	556	407	489
Th	3.10	2.77	3.61	3.80	3.22	4.55	4.74	4.18	3.89	4.66
U	1.42	1.33	1.24	1.73	0.77	1.00	1.01	1.35	0.84	1.04
Nb	75.5	73.0	45.3	92.5	39.8	48.2	48.9	52.6	44.4	53.9
Ta	2.06	2.14	3.16	2.70	3.26	3.49	3.31	3.68	3.08	2.58
K	9277	8548	9350	15,973	8395	13,591	13,592	14,177	11,383	12,311
Pb	3.76	3.34	4.04	4.32	3.21	3.61	5.45	3.29	3.36	6.11
Sr	958	1490	1220	1367	815	1023	1232	1377	868	1809
P	2396	2015	2326	2802	1906	2279	2305	2947	2012	2297
Zr	200	208	236	226	226	248	260	240	256	220
Hf	5.06	4.71	4.73	5.26	4.76	5.00	5.20	4.91	5.19	4.41
Ti	11,806	12,323	13,273	15,662	13,429	14,932	15,043	15,261	13,278	12,943
Y	23.13	23.84	26.70	25.67	25.84	27.38	27.23	28.93	28.58	25.71
V	201	185	213	220	200	222	212	226	200	200
Cr	176	194	188	27	313	41	44	36	71	44
Co	38.01	42.64	42.30	37.37	54.40	33.68	38.18	31.20	39.54	36.70
Ni	76.86	110.55	87.36	29.00	151.70	29.45	33.19	30.60		34.34
∑REE	167	164	176	189	167	192	196	199	186	166
Eu/Eu*	1.10	1.09	0.99	1.03	0.98	0.98	0.98	0.95	0.99	0.93
(La/Yb)n	8.96	8.48	8.77	8.73	9.18	9.81	9.68	9.97	8.88	9.45
$^{87}Rb/^{86}Sr$	0.0631257	0.029866	0.0484768	0.066006	0.0538877	0.087328	0.065463			
$^{87}Sr/^{86}Sr$	0.707152	0.708319	0.7076545	0.708030	0.706084	0.706911	0.707936			
2σ	9	9	4	8	7	9	9			
I_{Sr}	0.707044	0.7082768	0.707562	0.7079217	0.705992	0.706762	0.707824			
$^{147}Sm/^{144}Nd$	0.126222	0.119120	0.130744	0.117420	0.1204215	0.1195879	0.117312			
$^{143}Nd/^{144}Nd$	0.5127435	0.5128799	0.512724	0.5127219	0.512691	0.512742	0.512721			
2σ	6	7	2	1	2	5	3			
$\varepsilon_{Nd}(t)$	2.97	4.33	2.69	2.80	2.20	3.21	2.84			
2σ	0.12	0.14	0.04	0.02	0.04	0.10	0.06			

Sample	Lamprophyre								
	LM-1	LM-2	LM-3	LM-4	LM-5	JJHT-1	JJHT-2	JJHT-3	JJHT-4
Location	37°24′28.8″ 120°8′39.5″	37°23′52.8″ 120°8′1.8″	37°24′28.8″ 120°8′39.5″	37°23′52.8″ 120°8′1.8″	37°24′28.8″ 120°8′39.5″	37°23′52.8″ 120°8′1.8″	37°23′52.8″ 120°8′1.8″	37°23′52.8″ 120°8′1.8″	37°23′52.8″ 120°8′1.8″
Depth	331 m	415 m	127 m	163 m	295 m	432 m	245 m	112 m	239 m
SiO_2	46.35	45.67	50.07	47.12	44.69	46.57	46.36	45.98	47.06
TiO_2	1.76	1.93	1.83	2.37	2.09	2.10	2.16	2.22	2.07
Al_2O_3	15.60	16.54	13.03	16.05	15.49	16.48	14.29	14.07	15.84
TFe_2O_3	10.48	11.16	9.54	11.17	10.71	9.80	11.81	12.13	10.60
FeO	6.70	6.56	5.57	6.84	5.42	5.33	6.66	6.45	5.27

Table 1 (*continued*)

	Lamprophyre								
Sample	LM-1	LM-2	LM-3	LM-4	LM-5	JJHT-1	JJHT-2	JJHT-3	JJHT-4
Fe_2O_3	3.03	3.87	3.34	3.57	4.69	3.88	4.41	4.96	4.74
MnO	0.17	0.21	0.24	0.30	0.18	0.14	0.20	0.21	0.15
MgO	6.70	7.64	7.61	4.96	5.97	5.33	6.65	6.59	6.03
CaO	8.20	7.04	7.94	7.68	8.96	8.17	7.11	7.07	8.04
Na_2O	3.10	3.09	3.30	3.62	4.62	4.03	3.79	3.55	3.19
K_2O	2.51	2.54	2.22	2.78	3.04	2.85	2.84	3.10	2.89
P_2O_5	0.70	0.74	0.89	0.94	1.01	0.96	0.84	0.91	1.00
LOI	4.87	4.23	3.72	3.57	4.08	3.83	4.58	4.78	3.61
Total	99.7	100.1	99.8	99.8	100.2	99.7	99.9	99.9	99.9
Mg#	56	58	61	47	53	52	53	52	53
La	55.3	52.1	49.2	57.9	64.3	55.3	62.0	62.4	60.0
Ce	139.8	131.4	93.5	120.0	121.0	144.2	153.9	153.1	119.8
Pr	12.37	11.54	10.28	13.65	13.31	12.15	13.33	13.47	13.65
Nd	49.75	47.12	36.27	55.82	52.50	47.61	53.04	53.57	50.56
Sm	8.43	8.00	7.11	9.84	9.72	8.50	9.02	9.40	9.26
Eu	2.53	2.39	2.16	3.91	3.12	2.82	2.88	2.89	2.93
Gd	7.54	7.21	6.70	8.90	10.09	7.48	8.73	8.53	8.03
Tb	1.09	1.04	0.89	1.15	1.23	1.08	1.22	1.25	1.05
Dy	6.41	6.10	4.53	7.18	6.46	6.49	6.88	6.72	5.95
Ho	1.06	1.02	0.87	1.32	1.17	1.11	1.16	1.13	1.17
Er	3.11	2.96	2.30	3.33	3.14	3.05	3.31	3.26	2.93
Tm	0.44	0.42	0.30	0.47	0.40	0.45	0.48	0.43	0.40
Yb	2.60	2.42	1.96	2.98	2.58	2.52	2.75	2.59	2.48
Lu	0.36	0.38	0.28	0.42	0.38	0.38	0.39	0.41	0.38
Rb	92.20	116.38	83.42	90.38	86.46	74.83	97.98	114.36	75.23
Ba	956	693	483	484	1099	905	1002	1083	893
Th	7.33	7.12	7.76	9.46	10.19	7.53	8.76	8.65	8.07
U	3.14	3.15	1.72	2.96	2.83	3.29	4.04	3.80	2.55
Nb	168.4	165.8	87.9	99.5	105.9	172.7	190.4	206.6	101.0
Ta	4.88	4.78	4.18	7.36	6.05	5.26	5.64	5.72	6.78
K	21,823	21,783	19,083	23,798	26,045	23,151	23,318	25,453	23,236
Pb	5.28	6.31	9.60	4.47	11.34	4.04	3.99	4.58	4.11
Sr	1608	901	911	495	4225	1453	1451	1708	1449
P	3182	3351	4007	4223	4553	4104	3668	3973	4279
Zr	301	282	213	303	332	298	316	352	314
Hf	6.12	5.63	4.70	5.68	7.90	6.22	6.53	6.43	5.70
Ti	12,224	12,523	8406	13,355	12,588	12,360	12,960	13,320	12,180
Y	30.60	29.15	22.99	33.72	25.64	30.10	32.00	32.37	31.87
V	166	145	109	151	181	156	169	153	153
Cr	128	102	84	107	114	115	96	76	110
Co	36.29	26.74	31.12	40.06	35.83	33.26	35.90	33.04	33.35
Ni	114.03	104.51	90.08	136.79	83.03	104.10	73.14	69.39	115.10
∑REE	291	274	216	287	289	293	319	319	279
Eu/Eu^*	0.95	0.94	0.94	1.25	0.94	1.06	0.97	0.97	1.02
(La/Yb)n	11.81	11.96	13.94	10.78	13.87	12.19	12.53	13.39	13.45
$^{87}Rb/^{86}Sr$	0.1659655		0.2650105	0.528311	0.0592216	0.1490659	0.195380		0.150231
$^{87}Sr/^{86}Sr$	0.7071988		0.7089897	0.7071325	0.707181	0.707084	0.706062		0.707455
2σ	8		12	5	9	5	8		3
I_{Sr}	0.7069105		0.7084545	0.706224	0.707080	0.706830	0.7057329		0.707199
$^{147}Sm/^{144}Nd$	0.102363		0.1184436	0.1065545	0.1118107	0.107872	0.1027436		0.110659
$^{143}Nd/^{144}Nd$	0.512553		0.5125985	0.5127698	0.5126436	0.5126215	0.512654		0.512577
2σ	2		2	8	16	3	3		5
$\varepsilon_{Nd}(t)$	−0.21		0.16	2.55	1.26	0.91	1.75		0.13
2σ	0.04		0.04	0.16	0.31	0.06	0.06		0.10

Sample	JJHT-5	JJHT-6	JJHT-7	JJHT-8	JJHT-9	JJHT-10
Location	37°23′52.8″ 120°8′1.8″	37°23′52.8″ 120°8′1.8″	37°23′52.8″ 120°8′1.8″	37°23′52.8″ 120°8′1.8″	37°23′52.8″ 120°8′1.8″	37°23′52.8″ 120°8′1.8″
Depth	405 m	279 m	310 m	233 m	135 m	195 m
SiO_2	46.43	45.91	46.97	46.03	45.22	45.41
TiO_2	2.26	2.32	1.97	2.35	2.23	2.19
Al_2O_3	15.96	15.18	14.95	15.40	15.19	14.74
TFe_2O_3	11.25	12.05	10.55	11.62	11.05	11.01
FeO	6.28	5.84	5.33	6.75	6.55	7.20
Fe_2O_3	4.27	5.56	4.63	4.12	3.77	3.01
MnO	0.20	0.21	0.18	0.20	0.19	0.19
MgO	6.65	6.25	5.94	7.53	6.22	7.58
CaO	8.33	7.82	9.25	8.16	7.68	8.10
Na_2O	3.74	3.48	2.40	4.04	4.03	3.76
K_2O	2.84	3.29	2.89	2.75	2.69	2.52
P_2O_5	0.89	1.02	0.95	0.72	1.12	0.85
LOI	2.19	3.10	4.65	2.16	4.93	4.11
Total	100.0	100.0	100.1	100.2	99.8	99.7

(*continued on next page*)

Table 1 (*continued*)

Sample	JJHT-5	JJHT-6	JJHT-7	JJHT-8	JJHT-9	JJHT-10
Mg#	54	51	53	56	53	58
La	60.5	68.6	60.3	58.0	57.2	60.1
Ce	119.3	135.5	114.0	116.8	145.2	106.2
Pr	12.81	13.84	12.50	13.08	12.64	11.78
Nd	49.14	54.37	48.89	52.41	51.58	44.01
Sm	9.29	9.86	9.23	9.81	9.05	8.67
Eu	2.89	3.33	2.85	3.14	3.03	2.76
Gd	7.99	9.45	7.98	8.64	8.37	7.92
Tb	1.02	1.23	0.97	1.10	1.18	1.05
Dy	6.04	6.80	5.39	6.42	6.56	5.56
Ho	1.14	1.30	1.01	1.15	1.17	1.06
Er	2.97	3.31	2.54	3.08	3.17	2.76
Tm	0.40	0.44	0.36	0.40	0.46	0.38
Yb	2.52	2.84	2.26	2.52	2.64	2.53
Lu	0.38	0.41	0.35	0.38	0.38	0.34
Rb	75.22	90.99	77.77	85.42	89.70	72.64
Ba	1004	982	907	964	929	959
Th	8.36	10.25	8.02	9.42	8.57	9.70
U	2.77	3.25	2.65	2.05	3.53	2.11
Nb	101.8	117.7	97.9	90.5	182.1	109.9
Ta	6.81	8.16	6.62	6.75	5.86	5.43
K	22,579	26,192	22,497	21,840	22,086	20,911
Pb	4.71	3.59	4.27	5.71	4.38	5.62
Sr	1648	2076	1175	2652	1502	2605
P	3755	4323	3930	3056	4890	3711
Zr	309	340	290	317	331	275
Hf	5.36	6.42	5.22	5.60	6.63	5.66
Ti	13,140	13,500	11,220	13,620	13,380	13,140
Y	32.52	33.26	29.83	32.77	32.41	30.18
V	174	150	133	174	158	169
Cr	97	78	95	111	89	111
Co	36.00	33.07	30.93	38.45	32.44	36.10
Ni	111.10	72.10	109.14	125.73	69.44	112.83
∑REE	276	311	269	277	303	255
Eu/Eu*	1.01	1.03	1.00	1.02	1.04	1.00
(La/Yb)n	13.34	13.43	14.82	12.79	12.04	13.21
$^{87}Rb/^{86}Sr$	0.132073	0.1268325	0.1915219	0.093191	0.1728106	
$^{87}Sr/^{86}Sr$	0.705940	0.705681	0.706042	0.7065656	0.705824	
2σ	8	10	4	4	4	
I_{Sr}	0.7057215	0.7054765	0.7057215	0.7064397	0.7055329	
$^{147}Sm/^{144}Nd$	0.1142326	0.109573	0.1140769	0.113094	0.106011	
$^{143}Nd/^{144}Nd$	0.5125985	0.5126216	0.512532	0.51259	0.512641	
2σ	7	2	3	2	4	
$\varepsilon_{Nd}(t)$	0.23	0.91	−0.80	0.40	1.45	
2σ	0.14	0.04	0.0	0.0	0.08	

Mg# = 100 × molar Mg/(Mg + Fe).
$\lambda_{Rb} = 1.393 \times 10^{-11}$ year^{-1} (Nebel et al., 2011); $\lambda_{Sm} = 6.54 \times 10^{-12}$ year^{-1} (Lugmair and Marti, 1978); $\lambda_{U238} = 1.55125 \times 10^{-10}$ year^{-1}; $\lambda_{U235} = 9.8485 \times 10^{-10}$ year^{-1}; $\lambda_{Th232} = 4.9475 \times 10^{-11}$ year^{-1} (Steiger and Jäger, 1977).
$(^{147}Sm/^{144}Nd)_{CHUR} = 0.1967$ (Jacobsen and Wasserburg, 1980); $(^{143}Nd/^{144}Nd)_{CHUR} = 0.512638$ (Goldstein et al., 1984).
$(^{143}Nd/^{144}Nd)_{DM} = 0.513151$, $(^{147}Sm/^{144}Nd)_{DM} = 0.2136$ (Liew and Hofmann, 1988).
Samples JJHT-1 to −10 are from Ma et al. (2014a).

element contents are normalized to 100% on LOI (loss on ignition)-free basis in all related diagrams.

The lamprophyres and diabase-porphyries have similar SiO_2 (46.2–51.8 wt.%), Al_2O_3 (13.5–17.2 wt.%) and CaO (7.3–9.7 wt.%) contents. The lamprophyres have total alkali ($Na_2O + K_2O$) contents of 5.5–7.9 wt.%, and are classified as tephrite to trachybasalt, with only one sample plotting in the area of basaltic trachyandesite (Middlemost, 1994) (Fig. 3a). In contrast, the diabase-porphyries have relatively low total alkali contents of 4.2–6 wt.%, plotting in the fields of trachybasalt to basalt. The lamprophyres show high K_2O (2.3–3.4 wt.%) and K_2O/Na_2O (0.7–1.2 wt.%) and generally belong to the shoshonitic series, whereas the diabase-porphyries (K_2O = 1–1.9 wt.%; K_2O/Na_2O = 0.3–0.5 wt.%) are mainly calc-alkaline to high-K calc-alkaline rocks (Fig. 3b and c). Both types of rocks have high TiO_2 (1.8–2.5 wt.%) and total Fe_2O_3 (9.9–13.6 wt.%) contents (Fig. 3d).

In chondrite-normalized REE patterns (Fig. 4a), both the lamprophyres and diabase-porphyries are characterized by a moderate light rare-earth element (LREE) enrichment [$(La/Yb)_N$ = 8.5–13.9], without significant Eu anomalies (Eu/Eu* = 0.94–1.18). But the lamprophyres exhibit somewhat higher ΣREE contents and $(La/Yb)_N$ ratios than those of diabase-porphyries. Normalized trace element patterns of the lamprophyres resemble those of the diabase-porphyries, but the lamprophyres have higher incompatible element contents (Fig. 4b). Both rock types exhibit typical ocean island basalts (OIB) characteristics in terms of enrichment in Nb and Ta, and depletion in K and Pb, relative to LREE, except for two lamprophyre samples showing slight positive Pb anomalies. However, they also show negative Zr, Hf, and Ti anomalies (Hf/Hf* = 0.61–0.94, Ti/Ti* = 0.43–0.85) and positive Sr anomalies as well as superchondritic Zr/Hf ratios [39.6–57.6; compared with the chondritic Zr/Hf = 38 (Anders and Grevesse, 1989)].

As shown in the $^{87}Sr/^{86}Sr(t)$ vs. $\varepsilon_{Nd}(t)$ diagram (Fig. 5), the lamprophyres have variable initial $^{87}Sr/^{86}Sr$ ratios of 0.705465 to 0.708445 and uniform $\varepsilon_{Nd}(t)$ values of −0.8 to 2.6. The diabase-porphyries show similar Sr–Nd isotopic compositions to the lamprophyres, exhibiting initial $^{87}Sr/^{86}Sr$ = 0.705992–0.708268 and $\varepsilon_{Nd}(t)$ = 2.2–4.3.

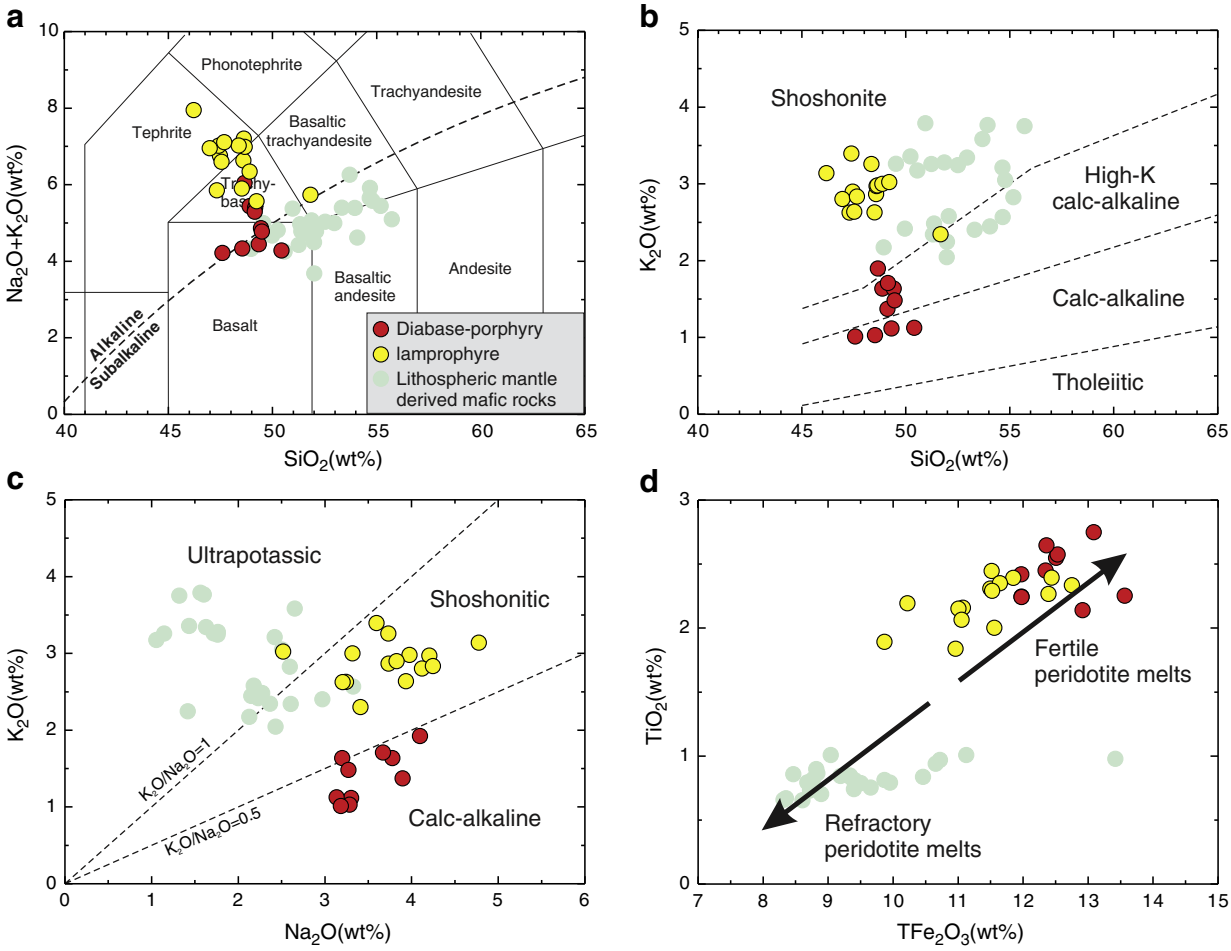

Fig. 3. (a) ($K_2O + Na_2O$) vs. SiO_2 diagram for classification of the mafic dikes in the Jiaodong Peninsula (Middlemost, 1994). (b) K_2O vs. SiO_2 classification diagram. (c) K_2O vs. Na_2O classification diagram. (d) Plot of TiO_2 vs. total Fe_2O_3, the fields of the peridotitic melts reported by Falloon et al. (1988). The lithospheric mantle-derived mafic rocks are from Ma et al. (2014a, 2014b).

4.2. Zircon U–Pb age and Hf isotope

The diabase-porphyry samples DP-2 and DP-5 were selected for zircon U–Pb dating. The data are listed in Table 2. Zircon CL images and U–Pb concordia diagrams are shown in Fig. 6. Zircon grains from these two samples are generally euhedral, long-prismatic and range in size from 70 to 130 μm, with length to width ratios of about 1.5:1 to 2.5:1. Based on CL images, magmatic oscillatory zoning is generally weak, with some of the zircon grains not showing any oscillatory zoning, which is quite different from the zircon in the host Linglong granite (160–157 Ma; Ma et al., 2013), but is typical of the zircon grains crystallized from mafic magma. Also no residual cores are observed in the crystals. The zircon grains exhibit large ranges of Th (118–1256 ppm) and U (137–1336 ppm) contents, with Th/U ratios varying from 0.32 to 1.78, suggesting a magmatic origin. The measured $^{206}Pb/^{238}U$ ages for the two diabase-porphyry samples are identical within analytical precision, yielding a weighted mean age of 122.4 ± 3.1 Ma (2σ, MSWD = 2.9, n = 9) for sample DP-2 and 122.6 ± 3.3 Ma (2σ, MSWD = 3.8, n = 9) for sample DP-5, respectively. We note in particular that there is no sign of any inherited zircon ages, either from the Precambrian basement or from the 160–157 Ma host granite. Thus the Early Cretaceous age of 123–122 Ma is interpreted to be the age of emplacement of the diabase-porphyry. The zircon U–Pb age of 122–121 Ma for the lamprophyre has previously been reported by Ma et al. (2014a). Within their limits of uncertainty, the diabase-porphyry and lamprophyre zircons have identical ages.

In-situ zircon Lu–Hf isotopes were also determined for the two diabase-porphyry samples DP-2 and DP-5 with corresponding U–Pb dating of the same domains. Analytical results are listed in Table 3, and the Hf isotopic histograms are also illustrated in Fig. 6. The $\varepsilon_{Hf}(t)$ values have been calculated at 120 Ma. Measured $^{176}Hf/^{177}Hf$ ratios for sample DP-2 are 0.282693 to 0.282761. Calculated $\varepsilon_{Hf}(t)$ values vary from −0.2 to 2.2 with a weighted mean of 1.3 ± 0.4 (2σ, MSWD = 0.9, n = 9), corresponding to T_{DM2} ages ranging from 1.04 Ga to 1.19 Ga. Sample DP-5 yielded $^{176}Hf/^{177}Hf$ ratios of 0.282675 to 0.282775. Calculated $\varepsilon_{Hf}(t)$ values vary from −0.9 to 2.7 with a mean $\varepsilon_{Hf}(t)$ of 1.4 ± 0.8 (2σ, MSWD = 2.5, n = 9). Overall, the Lu–Hf isotopic composition of two samples of the diabase-porphyry are in good agreement within the analytical precision, with both samples showing mostly positive $\varepsilon_{Hf}(t)$ values. The diabase-porphyry and lamprophyre also have the similar $\varepsilon_{Hf}(t)$ values (Ma et al., 2014a).

5. Discussion

5.1. Crustal contamination and fractional crystallization

Before trying to assess the mantle source characteristics and melting histories of the mafic rocks, we must consider the possible effects of crustal contamination during magma ascent. The lamprophyres and diabase-porphyries display “OIB-like” elemental and isotopic features, e.g., positive Nb and Ta anomalies, negative Pb anomalies and depleted Sr–Nd–Hf isotopes, all indicating negligible crustal contamination. The

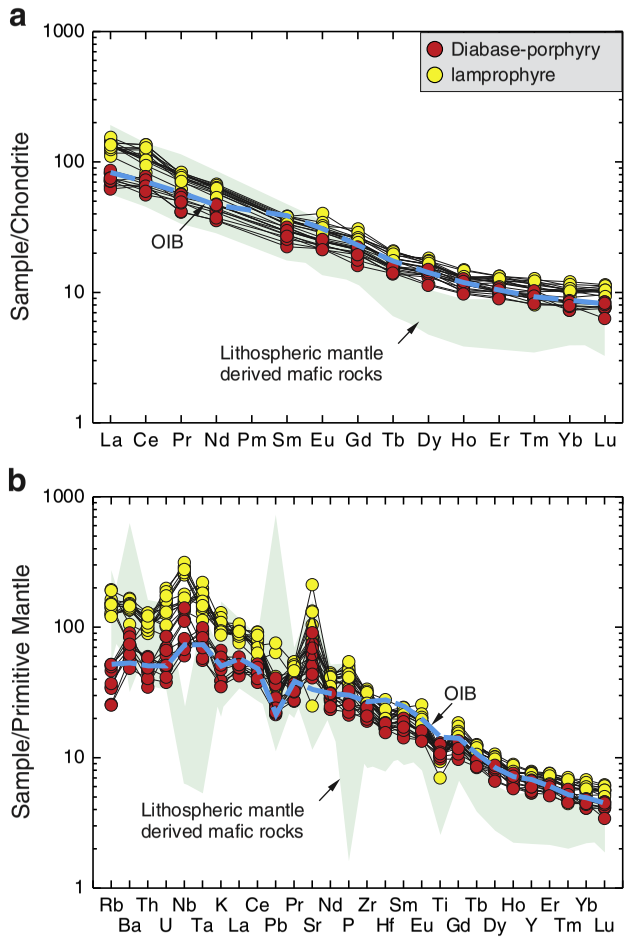

Fig. 4. (a) Chondrite-normalized REE pattern and (b) primitive mantle-normalized spider gram for the mafic dikes in the Jiaodong Peninsula. Data sources: Chondrites (Anders and Grevesse, 1989), primitive mantle (McDonough and Sun, 1995), the lithospheric mantle-derived mafic rocks (Ma et al., 2014a, 2014b).

canonical ratio Nb/U is a good parameter to estimate degrees of crustal contamination, because it is very sensitive to assimilate the crust materials. Hofmann et al. (1986) first noticed that uncontaminated fresh glasses of MORB and OIB have uniform Nb/U ratio of 47 ± 10 (see also

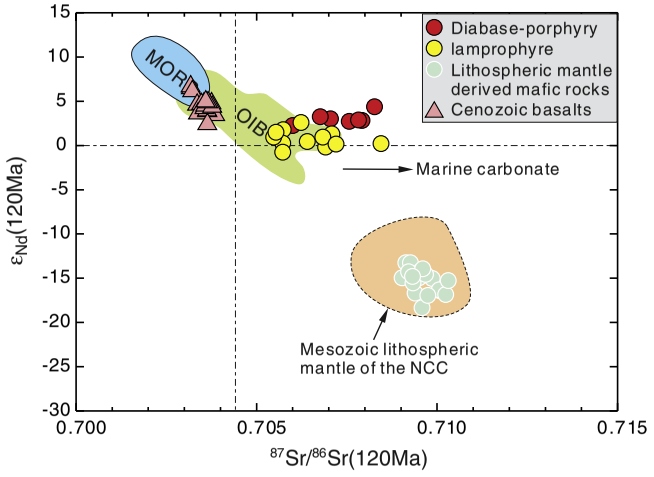

Fig. 5. Initial $^{87}Sr/^{86}Sr(t)$ vs. $\varepsilon_{Nd}(t)$ diagram for the mafic dikes in the Jiaodong Peninsula. Data sources: Mesozoic lithospheric mantle of the NCC (Guo et al., 2004; Yang et al., 2004; Ma et al., 2014a, 2014b), Cenozoic basalts (Zeng et al., 2011; Sakuyama et al., 2013), Marine carbonate (Shaw and Wasserburg, 1985), MORB and OIB (Zindler and Hart, 1986).

Table 2
LA-ICP-MS U–Pb isotopic data for the zircons from the diabase-porphyry in the Jiaodong Peninsula.

Spot	Th	U	Th/U	$^{207}Pb/^{206}Pb$	1σ	$^{207}Pb/^{235}U$	1σ	$^{206}Pb/^{238}U$	1σ	$^{208}Pb/^{232}Th$	1σ	$^{207}Pb/^{206}Pb$	1σ	$^{207}Pb/^{235}U$	1σ	$^{206}Pb/^{238}U$	1σ	$^{208}Pb/^{232}Th$	1σ
DP-2																			
1	220	339	0.65	0.05233	0.00229	0.13959	0.00589	0.01935	0.00035	0.00594	0.0003	300	63	133	5	124	2	120	6
2	170	294	0.58	0.04997	0.00286	0.13389	0.00739	0.01944	0.0004	0.00616	0.00038	194	90	128	7	124	3	124	8
3	118	238	0.50	0.04986	0.0041	0.12948	0.01028	0.01883	0.00048	0.00593	0.00053	188	132	124	9	120	3	120	11
4	145	298	0.49	0.04947	0.00347	0.13137	0.00889	0.01926	0.00044	0.00618	0.00048	170	112	125	8	123	3	125	10
5	282	551	0.51	0.04871	0.00476	0.13025	0.01222	0.0194	0.0006	0.00638	0.00065	134	152	124	11	124	4	129	13
6	160	500	0.32	0.05157	0.00155	0.13553	0.00355	0.01906	0.00028	0.00599	0.00009	266	71	129	3	122	2	121	2
7	383	771	0.50	0.04605	0.00238	0.12798	0.00637	0.02016	0.00029	0.00672	0.00132		112	122	6	129	2	135	27
8	243	137	1.78	0.04844	0.00399	0.12109	0.00981	0.01813	0.00036	0.00598	0.00054	121	144	116	9	116	2	121	11
9	246	379	0.65	0.04861	0.00195	0.12668	0.00505	0.0189	0.00031	0.00613	0.00316	129	63	121	5	121	2	124	63
DP-5																			
1	801	860	0.93	0.05377	0.00191	0.13594	0.00465	0.01834	0.00031	0.00545	0.00024	361	47	129	4	117	2	110	5
2	398	430	0.93	0.05158	0.00353	0.13175	0.00866	0.01853	0.00044	0.00539	0.00034	267	107	126	8	118	3	109	7
3	369	437	0.84	0.05279	0.00175	0.14234	0.00456	0.01956	0.00032	0.00613	0.00025	320	44	135	4	125	2	124	5
4	265	403	0.66	0.04744	0.00267	0.12862	0.007	0.01967	0.0004	0.00542	0.00033	71	83	123	6	126	3	109	7
5	669	805	0.83	0.05109	0.0007	0.12935	0.00179	0.01837	0.00025	0.00583	0.0002	245	14	124	2	117	2	117	4
6	416	920	0.45	0.05299	0.00149	0.14077	0.00383	0.01927	0.0003	0.00591	0.00027	328	34	134	3	123	2	119	5
7	627	432	1.45	0.04849	0.0018	0.13259	0.00478	0.01983	0.00033	0.0061	0.00023	123	54	126	4	127	2	123	5
8	143	301	0.47	0.05224	0.00227	0.14379	0.00604	0.01996	0.00036	0.00656	0.00037	296	63	136	5	127	2	132	7
9	1256	1336	0.94	0.04947	0.00347	0.13137	0.00889	0.01926	0.00044	0.00618	0.00048	170	112	125	8	123	3	125	10

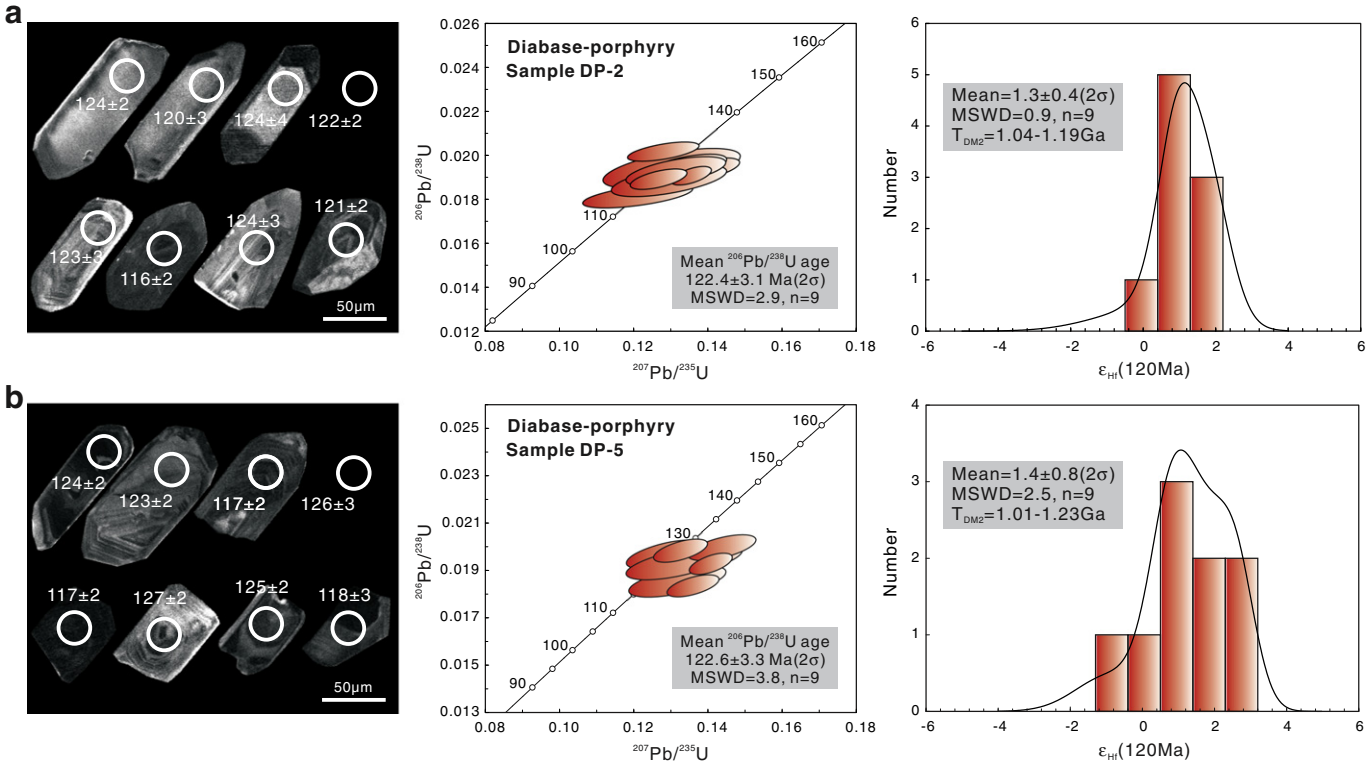

Fig. 6. Typical cathode luminescence images, LA-ICP-MS zircon U–Pb concordia diagrams and Histograms of zircon $\varepsilon_{Hf}(t)$ values for the diabase-porphyries in the Jiaodong Peninsula.

Hofmann, 2003), significantly higher than the value for average continental crust and arc volcanic rocks (Taylor and McLennan, 1985). As shown in Fig. 7a, our lamprophyres and diabase-porphyries have Nb/U ratios of 44.3 ± 10.6, typical of oceanic basalts, but significantly higher than those of the host granite (Nb/U = 9 ± 5; Ma et al., 2013), indicating that contamination, if it occurred at all, was generally insignificant. We also note in particular that there is no sign of any inherited zircon ages, either from the Precambrian basement or from the 160–157 Ma host granite. Thus, the effect of crustal contamination did not play a significant role on magma evolution of the lamprophyres and diabase-porphyries.

Fractional crystallization would be very difficult to detect in the lamprophyres and diabase-porphyries, because no obvious correlation is observed between MgO and most oxides, except for Al_2O_3 vs. MgO, and TiO_2 vs. MgO. The negative correlations between MgO and Al_2O_3 (Fig. 7b) and absence of Eu anomalies in the chondrite-normalized

Table 3
Zircon Hf isotopic compositions of the diabase-porphyry in the Jiaodong Peninsula.

Spot	$^{176}Yb/^{177}Hf$	$^{176}Lu/^{177}Hf$	$^{176}Hf/^{177}Hf$	2σ	εHf(0)	εHf(t)	2σ	t_{DM1}	t_{DM2}	$f_{Lu/Hf}$
DP-2										
1	0.019093	0.000886	0.282732	0.000014	−1.4	1.1	0.5	735	1102	−0.97
2	0.020195	0.000898	0.282725	0.000014	−1.6	0.9	0.5	744	1117	−0.97
3	0.015117	0.000677	0.282748	0.000013	−0.9	1.7	0.5	708	1065	−0.98
4	0.025915	0.001130	0.282761	0.000014	−0.4	2.2	0.5	698	1038	−0.97
5	0.025925	0.001112	0.282733	0.000016	−1.4	1.2	0.6	738	1102	−0.97
6	0.025192	0.001156	0.282731	0.000027	−1.4	1.1	0.9	741	1105	−0.97
7	0.024835	0.001081	0.282720	0.000015	−1.9	0.7	0.5	756	1131	−0.97
8	0.018997	0.000843	0.282741	0.000021	−1.1	1.5	0.7	721	1082	−0.97
9	0.023856	0.000951	0.282693	0.000037	−2.8	−0.2	1.3	791	1190	−0.97
DP-5										
1	0.017811	0.000805	0.282733	0.000017	−1.4	1.2	0.6	731	1099	−0.98
2	0.029558	0.001344	0.282675	0.000027	−3.4	−0.9	0.9	824	1231	−0.96
3	0.017128	0.000784	0.282775	0.000014	0.1	2.7	0.5	672	1005	−0.98
4	0.025498	0.001164	0.282722	0.000014	−1.8	0.8	0.5	754	1125	−0.96
5	0.048893	0.002004	0.282715	0.000016	−2.0	0.5	0.6	78	1145	−0.94
6	0.021641	0.000965	0.282768	0.000016	−0.1	2.4	0.6	685	1021	−0.97
7	0.032004	0.001308	0.282740	0.000022	−1.1	1.4	0.8	732	1087	−0.96
8	0.055246	0.002327	0.282753	0.000020	−0.7	1.8	0.7	733	1062	−0.93
9	0.035722	0.001838	0.282747	0.000020	−0.9	1.6	0.7	732	1074	−0.94

$e_{Hf}(t) = 10{,}000\{[(^{176}Hf/^{177}Hf)_S - (^{176}Lu/^{177}Hf)_S \times (e^{lt} - 1)] / [(^{176}Hf/^{177}Hf)_{CHUR,0} - (^{176}Lu/^{177}Hf)_{CHUR} \times (e^{lt} - 1)] - 1\}$.
$T_{DM1} = 1/l \times \ln\{1 + (^{176}Hf/^{177}Hf)S - (^{176}Hf/^{177}Hf)_{DM}] / [(^{176}Lu/^{177}Hf)_S - (^{176}Lu/^{177}Hf)_{DM}]\}$.
$T_{DM2} = 1/l \times \ln\{1 + [(^{176}Hf/^{177}Hf)_{S,t} - (^{176}Hf/^{177}Hf)_{DM,t}] / [(^{176}Lu/^{177}Hf)_C - (^{176}Lu/^{177}Hf)_{DM}]\} + t$.
The $^{176}Hf/^{177}Hf$ and $^{176}Lu/^{177}Hf$ ratios of chondrite and depleted mantle at the present are 0.282772 and 0.0332.
0.28325 and 0.0384, respectively (Blichert-Toft and Albarede, 1997; Griffin et al., 2000). $l = 1.867 * 10^{-11a-1}$.
(Söderlund et al., 2004) ($^{176}Lu/^{177}Hf)_C = 0.015$ (Griffin et al., 2002).

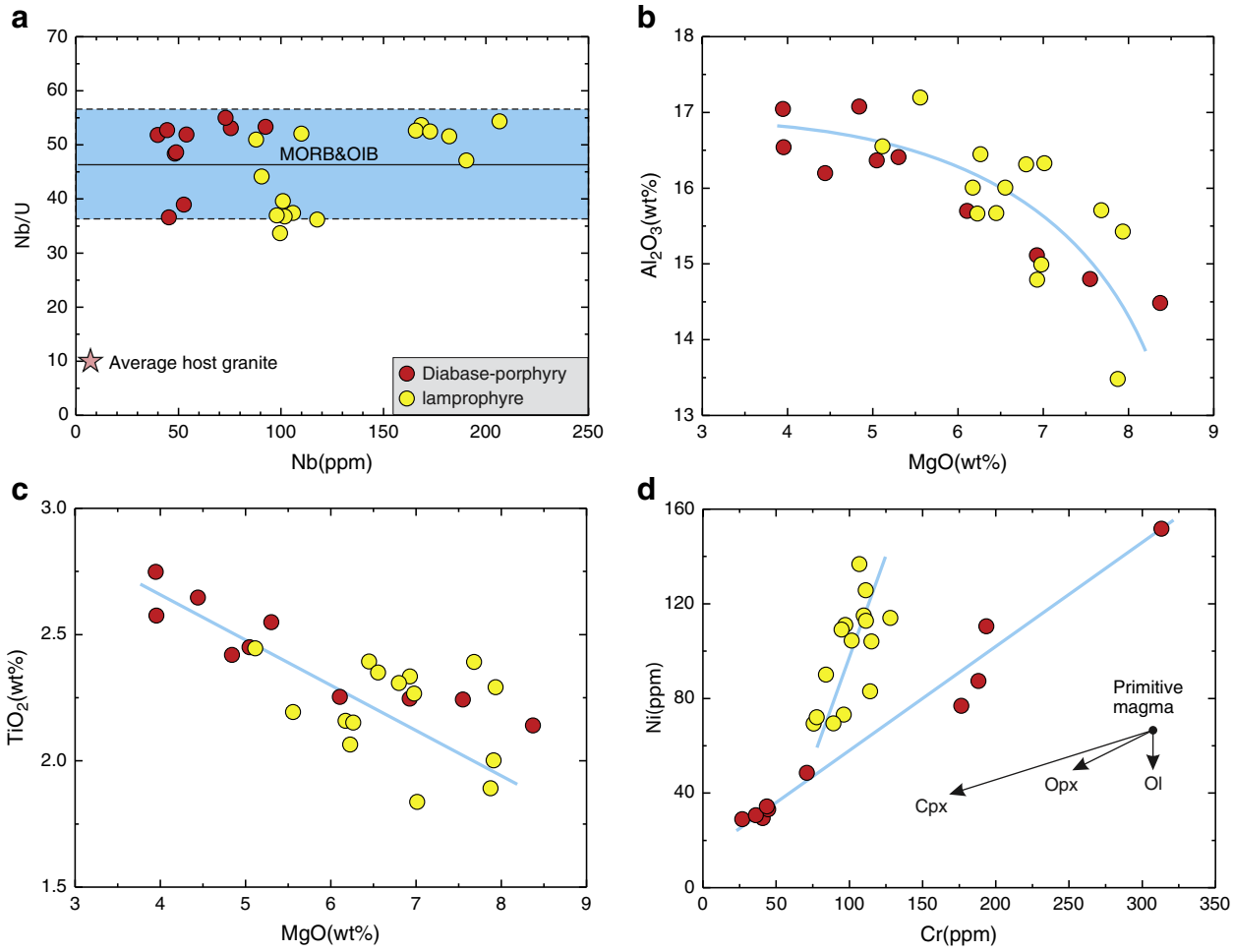

Fig. 7. (a) Plot of Nb/U vs. Nb for the mafic dikes in the Jiaodong Peninsula. The blue rectangle represents global MORB and OIB values (Hofmann et al., 1986); Average host granites are from Ma et al. (2013). (b) Al_2O_3 vs. MgO diagram. (c) TiO_2 vs. MgO diagram. (d) Ni vs. Cr diagram.

REE patterns (Fig. 4a) argue against significant fractionation of plagioclase. Likewise, fractionation of accessory minerals such as Fe–Ti oxides is insignificant as suggested by the clearly negative correlation between TiO_2 and MgO (Fig. 7c). However, in a plot of Ni vs. Cr (Fig. 7d), the lamprophyres and diabase-porphyries display two separate positive linear correlations with different slopes. In the diabase-porphyries, both Ni and Cr are strongly correlated with MgO (not shown), indicating that olivine fractionation with chromite coprecipitation (a phenomenon commonly observed in Hawaiian basalts) was important in this suite. In the lamprophyres no such correlations are apparent, Ni does not correlate with MgO, and the observed correlation between Ni and Cr remains enigmatic. Overall, it is clear, however, that the two type rocks do not represent fractionation products of a common parental magma.

5.2. Nature of mantle sources

The lamprophyres and diabase-porphyries show geochemical and isotopic features that are distinct from those of widespread lithospheric mantle-derived mafic rocks in the Jiaodong Peninsula. They are characterized by relatively high Ti and total Fe contents, and they resemble the field defined by experimental melts of fertile peridotite (Falloon et al., 1988), indicating that they are derived from a fertile mantle source (Fig. 3c). The trace element patterns with positive Nb–Ta and negative Pb anomalies are typical of normal ocean island basalts (Hofmann, 1997). Furthermore, these rocks also display typical OIB-like Sr–Nd and Hf isotopic compositions, indicating that they were derived from a convecting mantle. In the $^{87}Sr/^{86}Sr(t)$ vs. $\varepsilon_{Nd}(t)$ diagram (Fig. 5), our studied Cretaceous mafic dikes show more radiogenic Sr and slightly less radiogenic Nd isotopic compositions than those of Cenozoic basalts in the Jiaodong Peninsula (e.g., Zeng et al., 2011; Sakuyama et al., 2013), suggesting that more enriched components (EM2-type) had been incorporated into the mantle source of the lamprophyres and diabase-porphyries.

Because a similar asthenospheric origin with negligible crustal contamination has been inferred by the above discussion, the main differences in elemental geochemistry between the lamprophyres and diabase-porphyries are likely to result from different degrees of melting. REE inverse modeling calculation shows that variable degrees (2–5%) of batch melting of a hypothetical mantle source in the garnet stability field can generate the La/Sm–Sm/Yb compositions of the lamprophyres and diabase-porphyries (Fig. 8a). Specifically, the lamprophyres were generated by lower degree of melting (~2%) than the diabase-porphyries (~5%). These melting estimates are consistent with the different trace element features of the two rock types. The lamprophyres with lower degrees of melting have higher incompatible elements contents and $(La/Yb)_N$ ratios relative to the diabase-porphyries. Thus, the lamprophyres and diabase-porphyries were probably derived from partial melting of a fertile and convective asthenospheric mantle in the garnet stability field by different melting degrees.

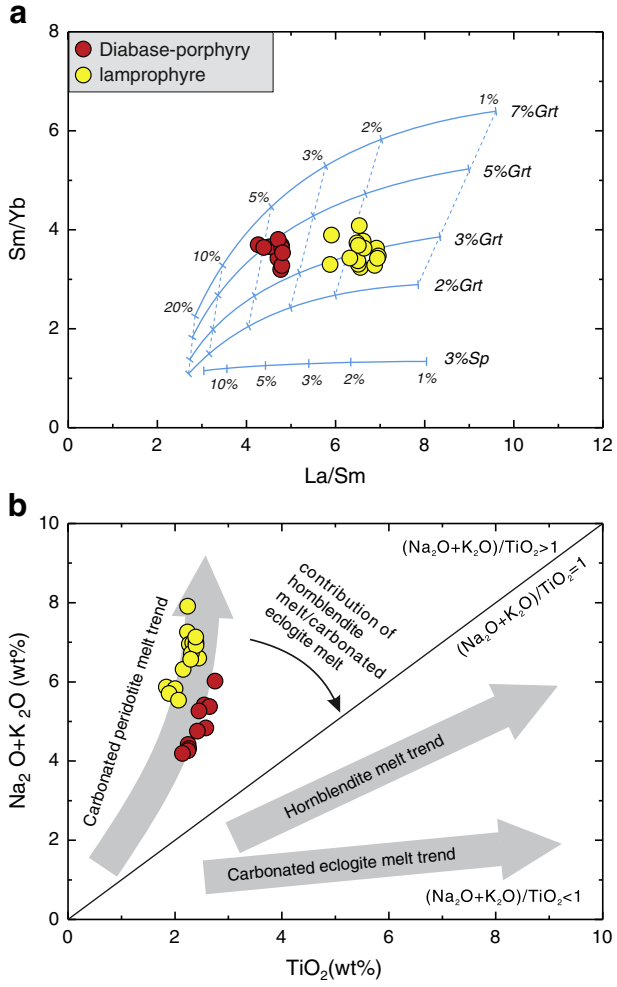

Fig. 8. (a) Variations in Sm/Yb vs. La/Sm for the mafic dikes in the Jiaodong Peninsula. Also shown are batch melting curves calculated for garnet peridotite and spinel peridotite. Partition coefficients are taken from McKenzie and O'Nions (1991). The melting curve of a spinel-bearing peridotite source: modal composition are 53% ol, 27% opx, 17% cpx, 3% sp.; melt mode are −6% ol, 28% opx, 67% cpx, 11% sp. (Kinzler, 1997). The melting curve of a garnet-bearing peridotite source: modal composition are 59–64% ol, 21% opx, 13% cpx, 7–2% grt; melt mode are 4% ol, −19% opx, 104% cpx, 11% grt (Hellebrand et al., 2002). (b) Plot of $Na_2O + K_2O$ vs. TiO_2 for the mafic dikes in the Jiaodong Peninsula and experimental alkaline melts. High-pressure experimental melts of the carbonated peridotite and eclogite, garnet pyroxenite, bimineralic eclogite, and hornblendite are from Zeng et al. (2010) and references therein.

5.3. A carbonated peridotite source?

Both the lamprophyres and diabase-porphyries exhibit negative Zr, Hf, and Ti anomalies relative to middle REEs and strongly elevated Zr/Hf ratios relative to chondritic value (see Fig. 4), suggesting that dry garnet peridotite is not a suitable source, because the bulk partition coefficients for Zr, Hf, and Ti between garnet peridotite and silicate melt are similar to those of middle REEs (Sm, Eu, and Gd) and also the peridotite has similar partition coefficients for Zr and Hf (Salters et al., 2002; Zeng et al., 2010). Previous studies on oceanic and continental carbonatites suggested that carbonatites are enriched in most incompatible elements except for K, Zr, Hf, and Ti, as well as having extremely high Zr/Hf and Ca/Al ratios (e.g., Hoernle and Tilton, 2002; Bizimis et al., 2003). Melting of a carbonated mantle will produce enriched melts with negative K, Zr, Hf, and Ti anomalies and supra-chondritic Zr/Hf ratios (Zeng et al., 2010). As shown in the plot of $Na_2O + K_2O$ vs. TiO_2 (Fig. 8b), the lamprophyres and diabase-porphyries plot in the field of $(K_2O + Na_2O)/TiO_2 > 1$, and define a well-correlated positive array that both Ti and total alkalis contents increase with decreasing degrees of melting. As the melting degrees decreased, the total alkalis contents increased much fast than the TiO_2 contents that are different from those of hornblendite and eclogite melt trend, but similar to those of carbonated peridotite melt trend (as reviewed by Zeng et al., 2010), indicating that carbonated peridotite may be the main source rock of the lamprophyres and diabase-porphyries.

The evidence for carbonated peridotite sources is somewhat equivocal, however, because the rather low CaO/Al_2O_3 ratios, which average 0.55 ± 0.06 and 0.52 ± 0.05, respectively, for the diabase-porphyry and the lamprophyre samples, whereas normally, one would expect significantly higher CaO and CaO/Al_2O_3 ratios in melts formed from carbonated peridotite sources. Another unexplained feature is the consistently positive Sr anomalies found in both rock types. Thus Sr/Nd ratios average 36 ± 12 in the diabase-porphyry dikes and 35 ± 17 (1 sigma std. deviation) in the lamprophyres, both of which are significantly higher than primitive-mantle values of $Sr/Nd = 16$ (McDonough and Sun, 1995). The uniformity of this Sr anomaly indicates that it is most likely intrinsic to the source rock rather than a product of unusual partitioning during partial melting. Positive Sr anomalies are not commonly observed in carbonatites, and experimentally determined peridotite carbonatite partition coefficients do not favor their formation during carbonate melting (e.g. Dasgupta et al., 2009). Nevertheless, some carbonatites found in China do have significant positive Sr anomalies. Among these are the carbonatites from Daluxiang and Maoniuping located at the western edge of the South China Block (Xu et al., 2010). High Sr/Nd has also been found in Cape Verde carbonatites by Doucelancea et al. (2010), where it appears that nearly all samples analyzed have Sr/Nd at least twice the primitive-mantle value. It seems likely that this Sr excess is a feature of the original carbonate, which may ultimately have been injected into the mantle by subduction. The Sr/Ca ratios of marine carbonates vary greatly, depending on whether the carbonate was precipitated as calcite or aragonite. Specifically, aragonite may have Sr contents of up to several thousand ppm (Coggon et al., 2004). Subduction of aragonite-dominated carbonate may therefore be the ultimate source of positive Sr anomalies in carbonatites and silicate melts derived from carbonated peridotite. We offer this as an admittedly speculative possibility. A recent report of sediment-derived carbonatite melt pockets in mantle xenoliths from Dalihu (northern China) by Liu et al. (2015) also shows distinct positive Sr anomalies and is thus consistent with the above speculation.

5.4. A possible lithospheric thinning model

It is well established that the lithosphere beneath the eastern NCC had been considerably thinned during late Mesozoic and early Cenozoic times (e.g., Menzies et al., 1993; Menzies and Xu, 1998; Griffin et al., 1998; Fan et al., 2000; Gao et al., 2002). However, the timing and manner of ancient lithosphere removal still remain controversial (Menzies et al., 2007; Wu et al., 2008; Xu et al., 2009; Zhu et al., 2011; Huang et al., 2012). The mechanism of lithospheric thinning has been interpreted in terms of either thermo-mechanical erosion or lithospheric delamination. These two models have different definitions and characteristics of magmatic activity. The thermo-mechanical–chemical erosion model suggests that the lowermost lithosphere is warmed conductively by the heat transported by upwelling asthenosphere and thus weakened and softened, so that it is then prone to be removed mechanically by lateral shear stresses in the asthenosphere. Progressive removal would ultimately result in lithospheric thinning (Jiang et al., 2010). Magmatism related to thermo-mechanical–chemical erosion is characterized by consumption of lithosphere at the beginning of lithospheric thinning. When the lithosphere has thinned to less than about 100 km, partial melting of the asthenosphere is initiated, generating asthenosphere derived magmas (Xu, 2001; Xu et al., 2004a, 2004b; Xu, 2006; Xu et al., 2009). In contrast, the lithospheric delamination model assumes that the thickened lower crust foundered together

with the subcrustal lithosphere and entered the underlying convecting mantle, thus causing much more rapid lithospheric thinning than in the lithospheric erosion model (Jiang et al., 2010). Magmatism related to lithospheric delamination would be rapid and short, and would be characterized by co-occurrence of lithospheric and asthenospheric mantle-derived magmas as well as crust-derived/mantle–crust mixed felsic magmas (Deng et al., 2007; Wu et al., 2008). The debate about these contrasting models has continued as to whether the mafic igneous activity was instantaneous and marked by rapid delamination lasting no more than 10 Myr, or whether it was part of a more protracted 100 Myr long transformation of the lithospheric keel (Menzies et al., 2007; Ma et al., 2014a).

The appearance of asthenosphere derived magmas and the magma source transition from lithospheric to asthenospheric mantle sources are considered to be two important signs of lithospheric thinning (Wu et al., 2008; Xu et al., 2009). However, the occurrences of asthenosphere-derived magmas during the Mesozoic in the NCC are extremely limited. Late Triassic dike swarms intruding the Liaodong Peninsula, northeastern China, have been interpreted to be derived from asthenospheric sources (Yang et al., 2007). However, although the isotopic compositions of these dikes resemble those of the Cretaceous lamprophyres discussed here, their trace element signatures are intermediate between clearly defined lithospheric and asthenospheric characteristics. Thus, the diagnostic trace element ratios of the Triassic "Group 1" rocks from Liaodong Peninsula average Nb/U = 31 ± 5 and Ce/Pb = 11 ± 3 and are thus significantly lower than the canonical mantle values of Nb/U = 47 ± 10 and Ce/Pb = 25 ± 6 (Hofmann et al., 1986). Yang et al. (2007) interpret these ratios as having been lowered from normal asthenospheric mantle values by crustal contamination. Although this is a reasonable interpretation, the involvement of a source with more lithospheric character seems equally likely, and in this sense the geochemical signals from the Triassic rocks are not clearly diagnostic. Three other places have been found recording the transition in magma source from a lithospheric to an asthenospheric mantle, including the Fuxin basalts (107–97 Ma) in the western Liaoning Province (Zhang et al., 2003b), the Daxizhuang alkali basalts (73 Ma) and Pishikou mafic dikes (86–78 Ma) in the Jiaodong Peninsula (Yan et al., 2003; Zhang et al., 2008b). Recently, we reported on earlier (122–121 Ma) asthenospheric mantle-derived lamprophyres in the Jiaodong Peninsula, clearly demonstrating the asthenosphere mantle melting during the Early Cretaceous (Ma et al., 2014a). Here, we have shown that the diabase dikes, which were generated by somewhat different degrees of melting and from slightly different asthenospheric source rocks, emplaced at the same time. Thus the more widespread eruption of asthenospheric magmas 123 to 121 Ma ago marks more clearly the end of lithosphere thinning of the NCC. As discussed earlier, normal asthenosphere unlikely to melt until the thickness of the lithosphere is considerably thinned, possibly to as much as 80 km (Mckenzie and Bickle, 1988). We note, however, that thinning to less than 80 km seems unlikely because all the asthenospheric melts have sufficiently steep HREE patterns to indicate that they were formed in the garnet peridotite stability field. In any case, the lamprophyres and diabase-porphyries represent the earliest asthenosphere-derived magma in the Jiaodong Peninsula, implying that lithospheric thinning beneath the Jiaodong Peninsula took place just prior to ~120 Ma.

The time and speed of the transition in magma sources (from lithospheric to asthenospheric mantle sources) are the two key questions in understanding the mechanisms for lithospheric thinning beneath the NCC. As shown in Fig. 9, the collision of the Yangtze Craton with the NCC took place in the Triassic (Li et al., 1993; Jahn et al., 1996; Zheng et al., 2003). The few Late Triassic syenite and mafic dikes in eastern Jiaodong are generally thought to represent a post-orogenic extensional regime resulting from such a collision (Yang et al., 2005; Zhao et al., 2012). The Palaeo-Pacific plate was subducted beneath the Eurasian continent before Jurassic time (Maruyama et al., 1997; Zhou and Li, 2000; Li and Li, 2007) This resulted in crustal thickening in eastern

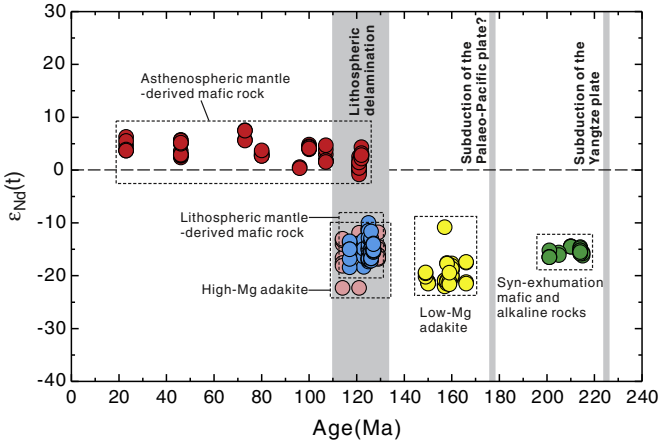

Fig. 9. Nd isotopic variation with time in Mesozoic and Cenozoic magmatic rocks. Data sources: Late Triassic syn-exhumation mafic and alkaline rocks (Yang et al., 2005; Zhao et al., 2012), Jurassic low-Mg adakatic granite (Hou et al., 2007b; Zhang et al., 2010; Yang et al., 2012; Ma et al., 2013), Cretaceous lithospheric and asthenospheric mantle-derived mafic rocks as well as high-Mg adakites (Yang et al., 2004; Guo et al., 2004; Tan et al., 2008; Liu et al., 2009; Ma et al., 2013, 2014a, 2014b), Cenozoic basalts (Yan et al., 2003; Zhang et al., 2003b; Zhang et al., 2008b; Kuang et al., 2009; Li et al., 2014).

China and partial melting of pre-existing ancient crust (Wu et al., 2005b), and the formation of low-Mg adakitic granites in the Jiaodong Peninsula such as the Linglong and Kunyushan granites (Hou et al., 2007b; Zhang et al., 2010; Yang et al., 2012; Ma et al., 2013). During the Early Cretaceous, large-scale magmatism occurred within a short period, including both lithospheric and asthenospheric mantle-derived mafic rocks as well as high-Mg adakites (Yang et al., 2004; Guo et al., 2004; Tan et al., 2008; Liu et al., 2008, 2009; Ma et al., 2013, 2014a, 2014b). After this period, all magmas were sourced in the asthenosphere, and magmatism within the lithosphere became nearly extinct (Yan et al., 2003; Zhang et al., 2003b; Zhang et al., 2008b; Kuang et al., 2009; Li et al., 2014). Thus, the transition from lithospheric to asthenospheric mantle sources took place about 120 Ma ago, and this transition was a relatively rapid process, in ~10 Myr. Thus, the NCC probably experienced a catastrophic lithospheric thinning event at ca.120 Ma. Geophysical data show that the lithosphere today is very thin (60–100 km) beneath the Jiaodong Peninsula and Bohai Sea, but that it is 100–150 km thick in the surrounding areas (Huang and Zhao, 2004; Xu and Zhao, 2009; Chen et al., 2009; Tian et al., 2009). Coincidentally, Mesozoic asthenospheric mantle-derived mafic rocks are exclusively distributed in the Jiaodong Peninsula and on the northern margin of the Bohai Sea. It therefore appears that the Jiaodong and Bohai areas were the center of lithospheric thinning beneath the NCC. If true, the rapid lithospheric delamination of the Jiaodong Peninsula and Bohai Sea would have induced decompressional melting of upwelling asthenospheric mantle to generate asthenospheric mantle-derived magmas, while the subcontinental lithospheric mantle was heated by the underlying convective asthenosphere and underwent partial melting to generate lithospheric mantle-derived magmas. Underplating of these hot mafic magmas would result in remelting of the lower crust and magma mixing to generate the high-Mg adakites. The rapid lithospheric delamination of the Jiaodong Peninsula and Bohai Sea would thus induce thermo-mechanical erosion of surrounding area of the NCC. Thus, the large-scale lithospheric thinning of the NCC may have been initiated beneath the Jiaodong Peninsula and Bohai Sea and then propagated towards the interior of the continent (Fig. 10).

6. Conclusions

(1) The lamprophyres and diabase-porphyries in the Jiaodong Peninsula were derived by partial melting of the asthenospheric mantle in the garnet stability field at different extents of melting.

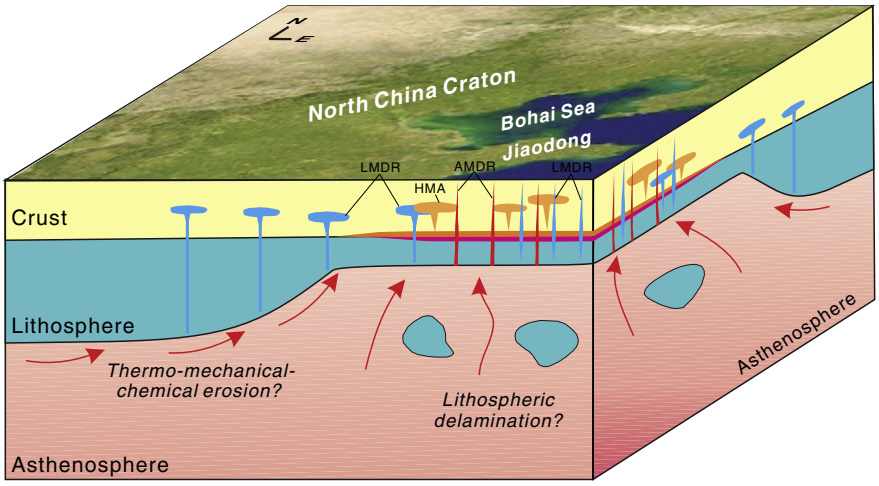

Fig. 10. A possible lithospheric thinning model for the NCC. Cartoon showing that the Jiaodong and Bohai area may have been the center of the lithospheric thinning beneath the NCC, where a rapid lithospheric delamination event began and induced upwelling of the convective asthenosphere. Partial melting of upwelling asthenosphere and subcontinental lithosphere simultaneously generated asthenospheric and lithospheric mantle-derived magmas. Underplating of these hot mafic magmas would result in remelting of the lower crust and magma mixing to generate the high-Mg adakites. The rapid lithospheric delamination of the Jiaodong Peninsula and Bohai Sea would induce concomitant thermo-mechanical erosion of surrounding area of the NCC, thus the large-scale lithospheric thinning of the NCC may have been initiated from the Jiaodong Peninsula and Bohai Sea and then propagated towards the interior of the continent. AMDR–asthenospheric mantle-derived rocks; LMDR–lithospheric mantle-derived rocks; HMA—high-Mg adakites.

Their mantle source had undergone enrichment with carbonatitic liquids, and the source rocks were mainly carbonated peridotite.

(2) Zircon LA-ICP-MS U–Pb dating indicates that these rocks were intruded at 123–121 Ma, and this makes them the earliest asthenosphere-derived magmas in the Jiaodong Peninsula.

(3) The co-occurrence of the asthenospheric and lithospheric mantle-derived mafic rocks as well as the high-Mg adakites indicates that the lithosphere beneath the Jiaodong Peninsula was rapidly delaminated just prior to ca. 120 Ma.

(4) Lithospheric thinning of the NCC may have been initiated from the Jiaodong Peninsula and Bohai Sea and then propagated towards the continental interiors.

Acknowledgments

We would like to thank two anonymous reviewers and Prof. Klaus Mezger for their critical and constructive reviews on our paper. We are also grateful to Prof. Jeffrey of University of South Florida for his help with written English. This study was supported by the China Postdoctoral Science Foundation (No. 2014M562218 and 2015T80922), the China National Science Foundation (No. 41503005 and 41172073), the External Cooperation Program of BIC, Chinese Academy of Sciences (No.132744KYSB20130005), the Chinese Ministry of Science and Technology 973 project (Grant 2006CB403506), and the State Key Laboratory of Isotope Geochemistry (Guangzhou Institute of Geochemistry, Chinese Academy of Sciences). This is publication No. IS-2214 from GIG-CAS.

References

Anders, E., Grevesse, N., 1989. Abundances of the elements: meteoritic and solar. Geochim. Cosmochim. Acta 53, 197–214.

Andersen, T., 2002. Correction of common lead in U–Pb analyses that do not report ^{204}Pb. Chem. Geol. 192, 59–79.

Bizimis, M., Salters, V.J.M., Dawson, J.B., 2003. The brevity of carbonatite sources in the mantle: evidence from Hf isotopes. Contrib. Mineral. Petrol. 145, 281–300.

Blichert-Toft, J., Albarede, F., 1997. The Lu–Hf isotope geochemistry of chondrites and the evolution of the mantle–crust system. Earth Planet. Sci. Lett. 148, 243–258.

Chen, L., Cheng, C., Wei, Z.G., 2009. Seismic evidence for significant lateral variations in lithospheric thickness beneath the central and western North China Craton. Earth Planet. Sci. Lett. 286, 171–183.

Chu, N.C., Taylor, R.N., Chavagnac, V., Nesbitt, R.W., Boella, R.M., Milton, J.A., German, C.R., Bayon, G., Burton, K., 2002. Hf isotope ratio analysis using multi-collector inductively coupled plasma mass spectrometry: an evaluation of isobaric interference corrections. J. Anal. At. Spectrom. 17, 1567–1574.

Coggon, R.M., Teagle, D.A.M., Cooper, M.J., Vanko, D.A., 2004. Linking basement carbonate vein compositions to porewater geochemistry across the eastern fank of the Juan de Fuca Ridge, ODP Leg 168. Earth Planet. Sci. Lett. 219, 111–128.

Dasgupta, R., Hirschmann, M.M., McDonough, W.F., Spiegelman, M., Withers, A.C., 2009. Trace element partitioning between garnet lherzolite and carbonatite at 6.6 and 8.6 GPa with applications to the geochemistry of the mantle and of mantle-derived melts. Chem. Geol. 262, 57–77.

Deng, J.F., Su, S.G., Niu, Y.L., Liu, C., Zhao, G.C., Zhao, X.G., Zhou, S., Wu, Z.X., 2007. A possible model for the lithospheric thinning of North China Craton: evidence from the Yanshanian (Jura-Cretaceous) magmatism and tectonism. Lithos 96, 22–35.

Doucelancea, R., Hammoudaa, T., Moreirad, M., Martinse, J.C., 2010. Geochemical constraints on depth of origin of oceanic carbonatites: the Cape Verde case. Geochim. Cosmochim. Acta 74, 7261–7282.

Elhlou, S., Belousova, E., Griffin, W.L., Pearson, N.J., O'Reilly, S.Y., 2006. Trace element and isotopic composition of GJ-red zircon standard by laser ablation. Geochim. Cosmochim. Acta 70, 158.

Falloon, T.J., Green, D.H., Hatton, C.J., Harris, K.L., 1988. Anhydrous partial melting of a fertile and depleted peridotite from 2 to 30 kb and application to basalt petrogenesis. J. Petrol. 29, 1257–1282.

Fan, W.M., Zhang, H.F., Baker, J., Jarvis, K.E., Mason, P.R.D., Menzies, M.A., 2000. On and off the North China Craton: where is the Archaean keel? J. Petrol. 41, 933–950.

Gao, S., Rudnick, R.L., Carlson, R.W., McDonough, W.F., Liu, Y.S., 2002. Re–Os evidence for replacement of ancient mantle lithosphere beneath the North China Craton. Earth Planet. Sci. Lett. 198, 307–322.

Gao, J.F., Lu, J.J., Lai, M.Y., Lin, Y.P., Pu, W., 2003. Analysis of trace elements in rock samples using HR-ICPMS. Journal of Nanjing University (Natural Sciences) 39, 844–850 (In Chinese with English abstract).

Gao, S., Rudnick, R.L., Yuan, H.L., Liu, X.M., Liu, Y.S., Xu, W.L., Ling, W.L., Ayers, J., Wang, X.C., Wang, Q.H., 2004. Recycling lower continental crust in the North China Craton. Nature 432, 892–897.

Goldstein, S.L., O'Nions, R.K., Hamilton, P.J., 1984. A Sm–Nd isotopic study of atmospheric dusts and particulates from major river systems. Earth Planet. Sci. Lett. 70, 221–236.

Griffin, W.L., Zhang, A.D., O'Reilly, S.Y., Ryan, C.G., 1998. Phanerozoic evolution of the lithosphere beneath the Sino-Korean Craton. In: Flower, M., Chung, S.L., Lo, C.H., Lee, T.Y. (Eds.), Mantle Dynamics and Plate Interactions in East Asia. American Geophysical Union Geodynamics Series, pp. 107–126.

Griffin, W.L., Pearson, N.J., Belousova, E., Jackson, S.E., Van Achterbergh, E., O'Reilly, S.Y., Shee, S.R., 2000. The Hf isotope composition of cratonic mantle: LAM-MC-ICPMS analysis of zircon megacrysts in kimberlites. Geochim. Cosmochim. Acta 64, 133–147.

Griffin, W.L., Wang, X., Jackson, S.E., Pearson, N.J., O'Reilly, S.Y., Xu, X., Zhou, X., 2002. Zircon chemistry and magma mixing, SE China: in-situ analysis of Hf isotopes, Tonglu and Pingtan igneous complexes. Lithos 61, 237–269.

Guo, F., Fan, W.M., Wang, Y.J., Zhang, M., 2004. Origin of early cretaceous calc-alkaline lamprophyres from the Sulu orogen in Eastern China: implications for enrichment processes beneath continental collisional belt. Lithos 78, 291–305.

Guo, J.H., Chen, F.K., Zhang, X.M., Siebel, W., Zhai, M.G., 2005. Evolution of syn- to post-collisional magmatism from North Sulu UHP belt, Eastern China: zircon U–Pb geochronology. Acta Petrol. Sin. 21, 1281–1301 (in Chinese with English abstract).

Hellebrand, E., Snow, J.E., Hoppe, P., Hofmann, A.W., 2002. Garnet-field melting and late-stage refertilization in "residual" abyssal peridotites from the Central Indian Ridge. J. Petrol. 12, 2305–2338.
Hoernle, K., Tilton, G., Le Bas, M.J., Duggen, S., Garbe-Schonberg, D., 2002. Geochemistry of oceanic carbonatites compared with continental carbonatites: mantle recycling of oceanic crustal carbonate. Contrib. Mineral. Petrol. 142, 520–542.
Hofmann, A.W., 1997. Mantle geochemistry: the message from oceanic volcanism. Nature 385, 219–229.
Hofmann, A.W., 2003. Sampling mantle heterogeneity through oceanic basalts: isotopes and trace elements. Treatise on geochemistry 2, 61–101.
Hofmann, A.W., Jochum, K.P., Seufert, M., White, W.M., 1986. Nb and Pb in oceanic basalts: new constraints on mantle evolution. Earth Planet. Sci. Lett. 79, 33–45.
Hou, K.J., Li, Y.H., Zou, T.R., Qu, X.M., Shi, Y.R., Xie, G.Q., 2007a. Laser ablation–MC–ICP–MS technique for Hf isotope microanalysis of zircon and its geological applications. Acta Petrol. Sin. 23, 2595–2604 (In Chinese with English abstract).
Hou, M.L., Jiang, Y.H., Jiang, S.Y., Ling, H.F., Zhao, K.D., 2007b. Contrasting origins of late Mesozoic adakitic granitoids from the northwestern Jiaodong Peninsula, East China: implications for crustal thickening to delamination. Geol. Mag. 144, 619–633.
Hu, F.F., Fan, H.H., Yang, J.H., Zhai, M.G., Xie, L.W., Yang, Y.H., Liu, X.M., 2007. Petrogenesis of Gongjia gabbro-diorite in the Kunyushan area, Jiaodong Peninsula: constraints from petro-geochemistry, zircon U–Pb dating and Hf isotopes. Acta Petrol. Sin. 23, 369–380 (in Chinese with English abstract).
Huang, J.C., Zhao, D.P., 2004. Crustal heterogeneity and seismotectonics of the region around Beijing, China. Tectonophysics 385, 159–180.
Huang, X.L., Zhong, J.W., Xu, Y.G., 2012. Two tales of the continental lithospheric mantle prior to the destruction of the North China Craton: insights from early cretaceous mafic intrusions in Western Shandong, East China. Geochim. Cosmochim. Acta 96, 193–214.
Jackson, S.E., Pearson, N.J., Griffin, W.L., Belousova, E.A., 2004. The application of laser ablation-inductively coupled plasma-mass spectrometry to in situ U–Pb zircon geochronology. Chem. Geol. 211, 47–69.
Jacobsen, S.B., Wasserburg, G.J., 1980. Sm–Nd isotopic evolution of chondrites. Earth Planet. Sci. Lett. 50, 139–155.
Jahn, B.M., Cornichet, J., Cong, B.L., Yui, T.F., 1996. Ultrahigh-ε_{Nd} eclogites from an ultrahigh-pressure metamorphic terrain of China. Chem. Geol. 127, 61–79.
Jahn, B.M., Liu, D.Y., Wan, Y.S., Song, B., Wu, J.S., 2008. Archean crustal evolution of the Jiaodong Peninsula, China, as revealed by zircon SHRIMP geochronology, elemental and Nd-isotope geochemistry. Am. J. Sci. 308, 232–269.
Jiang, Y.H., Jiang, S.Y., Ling, H.F., Ni, P., 2010. Petrogenesis and tectonic implications of Late Jurassic shoshonitic lamprophyre dikes from the Liaodong Peninsula, NE China. Mineral. Petrol. 100, 127–151.
Jiang, N., Guo, J., Chang, G., 2013. Nature and evolution of the lower crust in the eastern North China Craton: a review. Earth Sci. Rev. 122, 1–9.
Kinzler, R.J., 1997. Melting of mantle peridotite at pressure approaching the spinel to garnet transition: application to mid-ocean ridge petrogenesis. J. Geophys. Res. 102, 853–874.
Kuang, Y.S., Pang, C.J., Hong, L.B., Zhong, Y.T., Xu, Y.G., 2009. Geochronology and geochemistry of the late cretaceous basalts in the Jiaolai Basin: constraints on lithospheric thinning and accretion beneath North China Craton. Geotecton. Metallog. 559–571 (In Chinese with English abstract).
Li, Z.X., Li, X.H., 2007. Formation of the 1300-km-wide intracontinental orogen and postorogenic magmatic province in Mesozoic South China: a flat-slab subduction model. Geology 35, 179–182.
Li, S.G., Xiao, Y.L., Liou, D.L., Chen, Y.Z., Ge, N.J., Zhang, Z.Q., Sun, S.S., Cong, B.L., Zhang, R.Y., Hart, S.R., Wang, S.S., 1993. Collision of the North China and Yangtse Blocks and formation of coesite-bearing eclogites: timing and processes. Chem. Geol. 109, 89–111.
Li, J.W., Bi, S.J., Vasconcelos, P., 2010. Mineralization and genesis of the Fanjiabu gold deposit in the Sulu ultrahigh pressure metamorphic terrain, with a comparison to the gold mineralization in the Jiaobei terrain. Geol. J. China Univ. 16, 125–142 (in Chinese with English abstract).
Li, H.Y., Huang, X.L., Guo, H., 2014. Geochemistry of Cenozoic basalts from the Bohai Bay Basin: implications for a heterogeneous mantle source and lithospheric evolution beneath the eastern North China Craton. Lithos 196, 54–66.
Liew, T.C., Hofmann, A.W., 1988. Precambrian crustal components, plutonic associations, plate environment of the Hercynian Fold Belt of Central Europe: indications from a Nd and Sr isotopic study. Contrib. Mineral. Petrol. 98, 129–138.
Liu, D.Y., Nutman, A.P., Compston, W., Wu, J.S., Shen, Q.H., 1992. Remnants of ≥ 3800 Ma crust in the Chinese part of the Sino-Korean Craton. Geology 20, 339–342.
Liu, S., Hu, R.Z., Gao, S., Feng, C.X., Qi, Y.Q., Wang, T., Feng, G.Y., Coulson, I.M., 2008. U–Pb zircon age, geochemical and Sr-Nd-Pb-Hf isotopic constraints on age and origin of alkaline intrusions and associated mafic dikes from Sulu orogenic belt, Eastern China. Lithos 106, 365–379.
Liu, S., Hu, R.Z., Gao, S., Feng, C.X., Yu, B.B., Feng, G.Y., Qi, Y.Q., Wang, T., Coulson, I.M., 2009. Petrogenesis of Late Mesozoic mafic dykes in the Jiaodong Peninsula, eastern North China Craton and implications for the foundering of lower crust. Lithos 113, 621–639.
Liu, Y.S., He, D.T., Gao, C.G., Foley, S., Gao, S., Hu, Z.C., Zong, K.Q., Chen, H.H., 2015. First direct evidence of sedimentary carbonate recycling in subduction-related xenoliths. Sci. Report. 5, 11547. http://dx.doi.org/10.1038/srep11547.
Ludwig, K.R., 2003. ISOPLOT 3.00: a Geochronology Toolkit for Microsoft Excel. Berkeley Geochronological Center Special Publication, Berkeley.
Lugmair, G.W., Marti, K., 1978. Lunar initial 143Nd/144Nd: differential evolution of the lunar crust and mantle. Earth Planet. Sci. Lett. 39, 349–357.
Ma, L., Jiang, S.Y., Dai, B.Z., Jiang, Y.H., Hou, M.L., Pu, W., Xu, B., 2013. Multiple sources for the origin of Late Jurassic Linglong adakitic granite in the Shandong Peninsula, Eastern China: Zircon U–Pb geochronological, geochemical and Sr–Nd–Hf isotopic evidence. Lithos 162-163, 251–263.
Ma, L., Jiang, S.Y., Hofmann, A.W., Dai, B.Z., Hou, M.L., Zhao, K.D., Chen, L.H., Li, J.W., Jiang, Y.H., 2014a. Lithospheric and asthenospheric sources of lamprophyres in the Jiaodong Peninsula: a consequence of rapid lithospheric thinning beneath the North China Craton? Geochim. Cosmochim. Acta 124, 250–271.
Ma, L., Jiang, S.Y., Hou, M.L., Dai, B.Z., Jiang, Y.H., Yang, T., Zhao, K.D., Pu, W., Zhu, Z.Y., Xu, B., 2014b. Geochemistry of early cretaceous calc-alkaline lamprophyres in the Jiaodong Peninsula: implication for lithospheric evolution of the eastern North China Craton. Gondwana Res. 25, 859–872.
Maruyama, S., Isozaki, Y., Kimura, G., Terabayashi, M., 1997. Paleogeographic maps of the Japanese Islands: plate tectonic synthesis from 750 Ma to the present. Island Arc 6, 121–142.
McDonough, W.F., Sun, S.S., 1995. The composition of the earth. Chem. Geol. 120, 223–253.
Mckenzie, D.P., Bickle, M.J., 1988. The volume and composition of melt generated by extension of the lithosphere. J. Petrol. 29, 625–679.
McKenzie, D.P., O'Nions, R.K., 1991. Partial melt distribution from inversion of rare earth element concentrations. J. Petrol. 5, 1021–1091.
Menzies, M.A., Xu, Y.G., 1998. Geodynamics of the North China Craton. In: Flower, M., Chung, S.L., Lo, C.H., Lee, T.Y. (Eds.), Mantle Dynamics and Plate Interactions in East Asia. American Geophysical Union Geodynamics Series, pp. 155–165.
Menzies, M.A., Fan, W.M., Zhang, M., 1993. Palaeozoic and Cenozoic lithoprobes and the loss of >120 km of Archaean lithosphere, Sino-Korean Craton, China. In: Prichard, H.M., Alabaster, T., Harris, N.B.W., Neary, C.R. (Eds.), Magmatic Processes and Plate Tectonics. Geological Society Special Publications, pp. 71–78.
Menzies, M.A., Xu, Y.G., Zhang, H.F., Fan, W.M., 2007. Integration of geology, geophysics and geochemistry: a key to understanding the North China Craton. Lithos 96, 1–21.
Middlemost, E.A.K., 1994. Naming materials in the magma/igneous rock system. Earth Sci. Rev. 37, 215–224.
Nebel, O., Scherer, E.E., Mezger, K., 2011. Evaluation of the 87Rb decay constant by age comparison against the U–Pb system. Earth Planet. Sci. Lett. 301, 1–8.
Pu, W., Zhao, K.D., Ling, H.F., Jiang, S.Y., 2004. High precision Nd isotope measurement by Triton TI mass spectrometry. Acta Geosci. Sin. 25, 271–274 (In Chinese with English abstract).
Pu, W., Gao, J.F., Zhao, K.D., Ling, H.F., Jiang, S.Y., 2005. Separation method of Rb–Sr, Sm–Nd using DCTA and HIBA. Journal of Nanjing University (Nature Sciences) 41, 445–450 (In Chinese with English abstract).
Qiu, Y.M., Groves, D.I., Mcnaughton, N.J., Wang, L.G., Zhou, T.H., 2002. Nature, age, and tectonic setting of granitoid-hosted, orogenic gold deposits of the Jiaodong Peninsula, eastern North China Craton, China. Mineral. Deposita 37, 283–305.
Sakuyama, T., Tian, W., Kimura, J.I., Fukao, Y., Hirahara, Y., Takahashi, T., Senda, R., Chang, Q., Miyazaki, T., Obayashi, M., Kawabata, H., Tatsumi, Y., 2013. Melting of dehydrated oceanic crust from the stagnant slab and of the hydratedmantle transition zone: constraints from Cenozoic alkaline basalts in Eastern China. Chem. Geol. 359, 32–48.
Salters, V.J.M., Longhi, J.E., Bizimis, M., 2002. Near solidus trace element partitioning at pressures up to 3.4 GPa. Geochemistry, Geophysics, Geosystems 3 http://dx.doi.org/10.1029/2001GC000148.
Shaw, H.F., Wasserburg, G.J., 1985. Sm-Nd in marine carbonates and phosphates: implications for Nd isotopes in seawater and crustal ages. Geochim. Cosmochim. Acta 49, 503–518.
Söderlund, U., Patchett, P.J., Vervoort, J.D., Isachsen, C.E., 2004. The 176Lu decay constant determined by Lu–Hf and U–Pb isotope systematics of precambrian mafic intrusions. Earth Planet. Sci. Lett. 219, 311–324.
Steiger, R.H., Jäger, E., 1977. Subcommission on geochronology: convention on the use of decay constants in geo-and cosmochronology. Earth Planet. Sci. Lett. 36, 359–362.
Sun, W.D., Ding, X., Hu, Y.H., Li, X.H., 2007. The golden transformation of the cretaceous plate subduction in the West Pacific. Earth Planet. Sci. Lett. 262, 533–542.
Tan, J., Wei, J.H., Guo, L.L., Zhang, K.Q., Yao, C.L., Lu, J.P., Li, H.M., 2008. LA–ICP–MS zircon U–Pb dating and phenocryst EPMA of dikes, Guocheng, Jiaodong Peninsula: implications for North China Craton lithosphere evolution. Sci. China Ser. D Earth Sci. 51, 1483–1500.
Tang, J., Zheng, Y.F., Wu, Y.B., Gong, B., 2006. Zircon SHRIMP U–Pb dating, C and O isotopes for impure marbles from the Jiaobei terrain in the Sulu orogen: implication for tectonic affinity. Precambrian Res. 144, 1–18.
Tang, J., Zheng, Y.F., Wu, Y.B., Gong, B., Liu, X.M., 2007. Geochronology and geochemistry of metamorphic rocks in the Jiaobei terrain: constraints on its tectonic affinity in the Sulu orogen. Precambrian Res. 152, 48–82.
Taylor, S.R., McLennan, S.M., 1985. The Continental Crust: Its Composition and Evolution. Blackwell Scientific, Oxford, pp. 57–72.
Tian, Y., Zhao, D.P., Sun, R.M., Teng, J.W., 2009. Seismic imaging of the crust and upper mantle beneath the North China Craton. Phys. Earth Planet. Inter. 2009, 169–182.
Wang, L.G., Qiu, Y.M., Mcnaughton, N.J., Groves, D.I., Luo, Z.K., Huang, J.Z., Miao, L.C., Liu, Y.K., 1998. Constraints on crustal evolution and gold metallogeny in the northwestern Jiaodong Peninsula, China, from SHRIMP U–Pb zircon studies of granitoids. Ore Geol. Rev. 13, 275–291.
Woolley, A.R., Bergman, S.C., Edgar, A.D., Le Bas, M.J., Mitchell, R.H., Rock, N.M.S., Scott Smith, B.H., 1996. Classification of lamprophyres, lamproites, kimberlites, and the kalsilitic, melilitic, and leucitic rocks. Can. Mineral. 34, 175–186.
Wu, F.Y., Ge, W.C., Sun, D.Y., Guo, C.L., 2003. Discussions on the lithospheric thinning in Eastern China. Earth Science Frontiers 10, 51–60 (in Chinese with English abstract).
Wu, F.Y., Lin, J.Q., Wilde, S.A., Zhang, X.O., Yang, J.H., 2005a. Nature and significance of the early cretaceous giant igneous event in Eastern China. Earth Planet. Sci. Lett. 233, 103–119.
Wu, F.Y., Yang, J.H., Wilde, S.A., Zhang, X.O., 2005b. Geochronology, petrogenesis and tectonic implications of Jurassic granites in the Liaodong Peninsula, NE China. Chem. Geol. 221, 127–156.
Wu, F.Y., Xu, Y.G., Gao, S., Zheng, J.P., 2008. Lithospheric thinning and destruction of North China Craton. Acta Petrol. Sin. 24, 1145–1174 (in Chinese with English abstract).

Xu, Y.G., 2001. Thermo-tectonic destruction of the Archaean lithospheric keel beneath the Sino-Korean craton in China: evidence, timing and mechanism. Phys. Chem. Earth Solid Earth Geod. 26, 747–757.
Xu, Y.G., 2006. Using basalt geochemistry to constrain Mesozoic-Cenozoic evolution of the lithosphere beneath North China Craton. Earth Science Frontiers 13, 93–104 (In Chinese with English abstract).
Xu, P.F., Zhao, D.P., 2009. Upper-mantle velocity structure beneath the North China Craton: implications for lithospheric thinning. Geophys. J. Int. 177, 1279–1283.
Xu, Y.G., Chung, S.L., Ma, J.L., Shi, L.B., 2004a. Contrasting Cenozoic lithospheric evolution and architecture in the Western and eastern Sino-Korean Craton: constraints from geochemistry of basalts and mantle xenoliths. J. Geol. 112, 593–605.
Xu, Y.G., Huang, X.L., Ma, J.L., Wang, Y.B., Iizuka, Y., Xu, J.F., Wang, Q., Wu, X.Y., 2004b. Crust–mantle interaction during the tectono-thermal reactivation of the North China Craton: constraints from SHRIMP zircon U–Pb chronology and geochemistry of Mesozoic plutons from Western Shandong. Contrib. Mineral. Petrol. 147, 750–767.
Xu, Y.G., Li, H.Y., Pang, C.J., He, B., 2009. On the timing and duration of the destruction of the North China Craton. Chin. Sci. Bull. 54, 3379–3396.
Xu, C., Wang, L.J., Song, W.L., Wu, M., 2010. Carbonatites in China: a review for genesis and mineralization. Geosci. Front. 1, 105–114.
Yan, J., Chen, J.F., Xie, Z., 2003. Mantle xenoliths from late cretaceous basalt in Eastern Shandong Province: new constraint on the timing of lithospheric thinning in Eastern China. Chin. Sci. Bull. 48, 2139–2144.
Yang, W., Li, S.G., 2008. Geochronology and geochemistry of the Mesozoic volcanic rocks in Western Liaoning: implications for lithospheric thinning of the North China Craton. Lithos 102, 88–117.
Yang, J.H., Wu, F.Y., 2009. Triassic magmatism and its relation to decratonization in the eastern North China Craton. Sci. China Ser. D Earth Sci. 52, 1319–1330.
Yang, J.H., Wu, F.Y., Wilde, S.A., 2003. A review of the geodynamic setting of large-scale Late Mesozoic gold mineralization in the North China Craton: an association with lithospheric thinning. Ore Geol. Rev. 23, 125–152.
Yang, J.H., Chung, S.L., Zhai, M.G., Zhou, X.H., 2004. Geochemical and Sr–Nd–Pb isotopic compositions of mafic dikes from the Jiaodong Peninsula, China: evidence for vein-plus-peridotite melting in the lithospheric mantle. Lithos 73, 145–160.
Yang, J.H., Chung, S.L., Wilde, S.A., Wu, F.Y., Chu, M.F., Lo, C.H., Fan, H.R., 2005. Petrogenesis of post-orogenic syenites in the Sulu Orogenic Belt, East China: geochronological, geochemical and Nd-Sr isotopic evidence. Chem. Geol. 214, 99–125.
Yang, J.H., Sun, J.F., Chen, F.K., Wilde, S.A., Wu, F.Y., 2007. Sources and petrogenesis of late Triassic dolerite dikes in the Liaodong Peninsula: implications for post-collisional lithosphere thinning of the eastern North China Craton. J. Petrol. 48, 1973–1997.
Yang, K.F., Fan, H.R., Santosh, M., Hu, F.F., Wilde, S.A., Lan, T.G., Lu, L.N., Liu, Y.S., 2012. Reactivation of the Archean lower crust: implications for zircon geochronology, elemental and Sr–Nd–f isotopic geochemistry of late Mesozoic granitoids from northwestern Jiaodong terrane, the North China Craton. Lithos 146, 112–127.
Zeng, G., Chen, L.H., Xu, X.S., Jiang, S.Y., Hofmann, A.W., 2010. Carbonated mantle sources for Cenozoic intra-plate alkaline basalts in Shandong, North China. Chem. Geol. 273, 35–45.
Zeng, G., Chen, L.H., Hofmann, A.W., Jiang, S.Y., Xu, X.S., 2011. Crust recycling in the sources of two parallel volcanic chains in Shandong, North China. Earth Planet. Sci. Lett. 302, 359–368.
Zhai, M.G., Santosh, M., 2011. The early Precambrian odyssey of the North China Craton: a synoptic overview. Gondwana Res. 20, 6–25.
Zhang, X.O., Cawood, P.A., Wilde, S.A., Liu, R.Q., Song, H.L., Li, W., Snee, L.W., 2003a. Geology and timing of mineralization at the Cangshang gold deposit, north-western Jiaodong Peninsula, China. Mineral. Deposita 38, 141–153.
Zhang, H.F., Sun, M., Zhou, X.H., Zhou, M.F., Fan, W.M., Zheng, J.P., 2003b. Secular evolution of the lithosphere beneath the eastern North China Craton: evidence from Mesozoic basalts and high-Mg andesites. Geochim. Cosmochim. Acta 67, 4373–4387.
Zhang, H.F., Goldstein, S.L., Zhou, X.H., Sun, M., Zheng, J.P., Cai, Y., 2008a. Evolution of subcontinental lithospheric mantle beneath Eastern China: Re–Os isotopic evidence from mantle xenoliths in Paleozoic kimberlites and Mesozoic basalts. Contrib. Mineral. Petrol. 155, 271–293.
Zhang, J., Zhang, H.F., Ying, J.F., Tang, Y.J., Niu, L.F., 2008b. Contribution of subducted Pacific slab to Late cretaceous mafic magmatism in Qingdao region, China: a petrological record. Island Arc 17, 231–241.
Zhang, J., Zhao, Z.F., Zheng, Y.F., Dai, M.N., 2010. Postcollisional magmatism: geochemical constraints on the petrogenesis of Mesozoic granitoids in the Sulu orogen, China. Lithos 119, 512–536.
Zhao, G.C., Wilde, S.A., Cawood, P.A., Sun, M., 2001. Archean blocks and their boundaries in the North China Craton: lithological, geochemical, structural and PT path constraints and tectonic evolution. Precambrian Res. 107, 45–73.
Zhao, Z.F., Zheng, Y.F., Zhang, J., Dai, L.Q., Li, Q.L., Liu, X.M., 2012. Syn-exhumation magmatism during continental collision: evidence from alkaline intrusives of Triassic age in the Sulu orogen. Chem. Geol. 328, 70–88.
Zheng, Y.F., Fu, B., Gong, B., Li, L., 2003. Stable isotope geochemistry of ultrahigh pressure metamorphic rocks from the Dabie–Sulu orogen in China: implications for geodynamics and fluid regime. Earth Sci. Rev. 62, 105–161.
Zheng, J.P., Griffin, W.L., O'Reilly, S.Y., Yang, J., Li, T., Zhang, M., Zhang, R.Y., Liou, J.G., 2006. Mineral chemistry of peridotites from Paleozoic, Mesozoic and Cenozoic lithosphere: constraints on mantle evolution beneath Eastern China. J. Petrol. 47, 2233–2256.
Zheng, J.P., Griffin, W.L., O'Reilly, S.Y., Yu, C.M., Zhang, H.F., Pearson, N., Zhang, M., 2007. Mechanism and timing of lithospheric modification and replacement beneath the eastern North China Craton: peridotitic xenoliths from the 100 Ma Fuxin basalts and a regional synthesis. Geochim. Cosmochim. Acta 71, 5203–5225.
Zhou, X.M., Li, W.X., 2000. Origin of Late Mesozoic igneous rocks in Southeastern China: implications for lithosphere subduction and underplating of mafic magmas. Tectonophysics 326, 269–287.
Zhu, R.X., Chen, L., Wu, F.Y., Liu, J.F., 2011. Timing, scale and mechanism of the destruction of the North China Craton. Sci. China Earth Sci. 54, 789–797.
Zindler, A., Hart, S., 1986. Chemical geodynamics. Annu. Rev. Earth Planet. Sci. 14, 493–571.